

Lawrence Berkeley National Laboratory

Recent Work

Title

DIFFERENTIAL CROSS SECTIONS FOR ELASTIC SCATTERING OF POSITIVE PI MESONS ON PROTONS IN THE ENERGY REGION 500 TO 1600 MeV

Permalink

<https://escholarship.org/uc/item/5388z5q9>

Author

Helland, Jerome A.

Publication Date

1962-08-15

UCRL-10378

Cy. 2

University of California
Ernest O. Lawrence
Radiation Laboratory

TWO-WEEK LOAN COPY

*This is a Library Circulating Copy
which may be borrowed for two weeks.
For a personal retention copy, call
Tech. Info. Division, Ext. 5545*

DIFFERENTIAL CROSS SECTIONS FOR ELASTIC
SCATTERING OF POSITIVE PI MESONS ON PROTONS
IN THE ENERGY REGION 500 TO 1600 MeV

Berkeley, California

UCRL-10378
Cy. 2

DISCLAIMER

This document was prepared as an account of work sponsored by the United States Government. While this document is believed to contain correct information, neither the United States Government nor any agency thereof, nor the Regents of the University of California, nor any of their employees, makes any warranty, express or implied, or assumes any legal responsibility for the accuracy, completeness, or usefulness of any information, apparatus, product, or process disclosed, or represents that its use would not infringe privately owned rights. Reference herein to any specific commercial product, process, or service by its trade name, trademark, manufacturer, or otherwise, does not necessarily constitute or imply its endorsement, recommendation, or favoring by the United States Government or any agency thereof, or the Regents of the University of California. The views and opinions of authors expressed herein do not necessarily state or reflect those of the United States Government or any agency thereof or the Regents of the University of California.

UCRL-10378
UC-34 Physics
TID-4500 (17th Ed)

UNIVERSITY OF CALIFORNIA
Lawrence Radiation Laboratory
Berkeley, California

Contract No. W-7405-eng-48

DIFFERENTIAL CROSS SECTIONS FOR ELASTIC SCATTERING
OF POSITIVE PI MESONS ON PROTONS
IN THE ENERGY REGION 500 TO 1600 MeV

Jerome A. Helland
(Thesis)

August 15, 1962

DIFFERENTIAL CROSS SECTIONS FOR ELASTIC SCATTERING
OF POSITIVE PI MESONS ON PROTONS
IN THE ENERGY REGION 500 TO 1600 MeV

Contents

Abstract	iv
I. Introduction	1
II. Experimental Method and Equipment	5
A. Experimental Method	5
B. Equipment	6
1. Source of Pions	6
2. Beam Design	8
3. Liquid-Hydrogen Target	16
4. Scintillation Counters	18
5. Electronics	27
6. Cerenkov Counter	35
III. Analysis of Data	
A. General Analysis	38
B. Corrections to Data	42
1. Inelastic Scattering	42
2. Accidentals	45
3. Reverse Elastics	47
4. Beam Contamination	50
5. Miscellaneous Corrections and Errors	51
IV. Experimental Results	
A. Differential-Cross-Section Data	55
B. Cosine Fits	55
C. Total Elastic Cross Sections	72
V. Discussion	77
Acknowledgments	82
Appendices	
A. Momentum Determination	84
B. Velocity-Spectrometer Equation	86
References	87

DIFFERENTIAL CROSS SECTIONS FOR ELASTIC SCATTERING
OF POSITIVE PI MESONS ON PROTONS
IN THE ENERGY REGION 500 TO 1600 MeV

Jerome A. Helland

Lawrence Radiation Laboratory
University of California
Berkeley, California

August 15, 1962

ABSTRACT

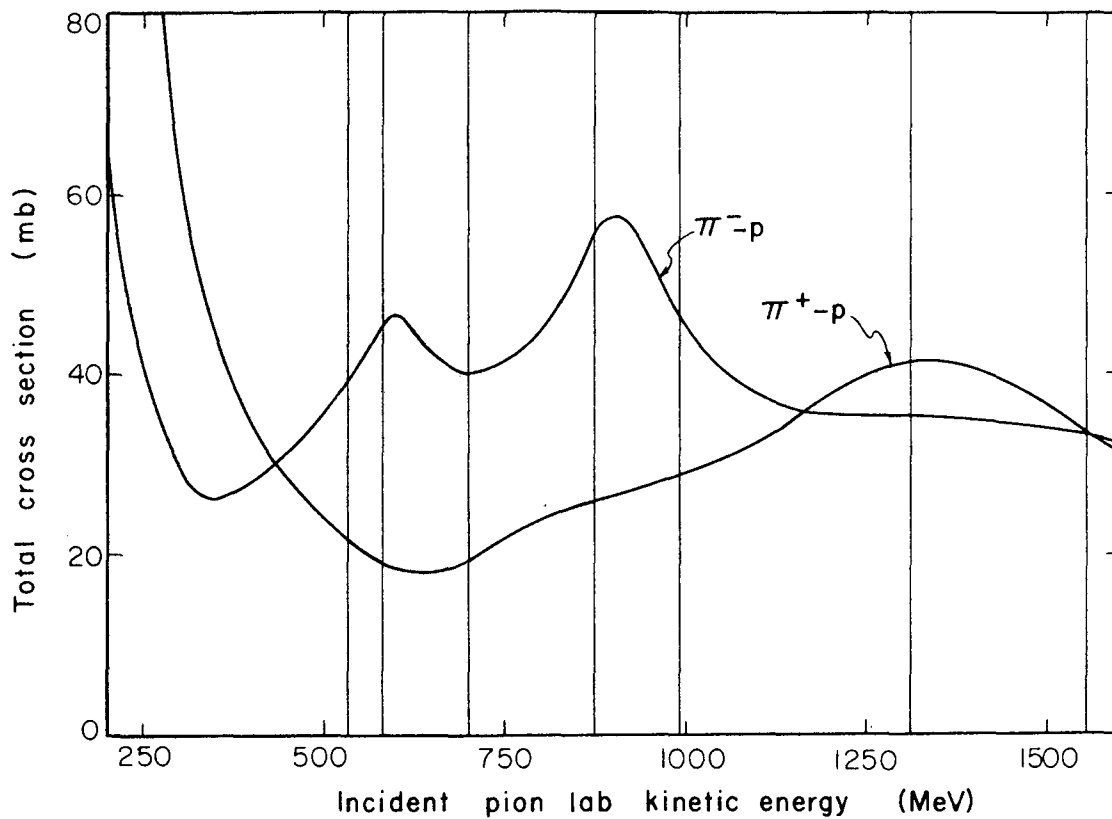
Differential cross sections for the elastic scattering of positive pi mesons on protons were measured at the Berkeley Bevatron at laboratory kinetic energies of the pion between 500 and 1600 MeV. Fifty scintillation counters and a matrix coincidence system were used to detect the recoil proton and the pion, both before the latter reached a liquid-hydrogen target and after scattering. Various corrections were applied to the data, and the results were fitted with a power series in the cosine of the scattering angle in the center-of-mass system. Total elastic cross sections were obtained by integrating under the fitted curves. The coefficients of the cosine series are shown plotted vs the laboratory kinetic energy of the pion. The most striking features of these curves are the large positive value of the coefficient of $\cos^6 \theta^*$, and the large negative value of the coefficient of $\cos^4 \theta^*$, both of which peaked in the vicinity of the 1350-MeV peak in the total cross section. These results indicate that the most predominant state contributing to the scattering at the 1350 MeV peak has total angular momentum $J = 7/2$, considering that the coefficients for terms above $\cos^6 \theta^*$ are negligible at this energy. One possible explanation is that the 1350-MeV peak is the result of an $F_{7/2}$ resonance lying on the same Regge-pole trajectory as the famous (3, 3) resonance near 195 MeV.

I. INTRODUCTION

In this experiment the differential cross sections for the elastic scattering of positive pi mesons (pions) on protons were measured at incident pion laboratory kinetic energies between 500 and 1600 MeV. Although considerable work has been done in the study of π^- -p scattering,¹ little has been done on π^+ -p scattering in this energy range. Several bubble-chamber experiments have been performed within the past few years to measure the π^+ -p differential cross sections (d.c.s.). Bidan et al., using the Saclay propane bubble chamber, measured the d.c.s. at 1000 MeV.^{2a} Barloutaud et al., using the Saclay hydrogen bubble chamber, measured the d.c.s. at 820, 900, and 1050 MeV.^{2b} Kopp et al., using a hydrogen bubble chamber at the Brookhaven Cosmotron, measured the d.c.s. at 990 MeV.^{2c} Roellig and Glaser using a propane bubble chamber at Michigan, measured the d.c.s. at 1100 MeV.^{2d} This work is also discussed in reference 2e. Willis, using a hydrogen bubble chamber at Brookhaven, measured the d.c.s. at 500 MeV.^{2f} In most of these experiments the π^+ -p d.c.s. is based on 200 to 1200 events per energy.

This experiment was performed as a more detailed study of various phenomena that were originally observed in the total cross sections, as measured by several experimental groups within the past few years.³ The first phenomenon that was discovered was the famous (3, 3) resonance, which has a total energy of about 1238 MeV in the center-of-mass (c.m.) system. This resonance has been studied quite thoroughly and the quantum numbers associated with the resonant state are well known. The (3, 3) resonance has isotopic spin $T = 3/2$, total angular momentum $J = 3/2$, orbital angular momentum $l = 1$, and positive parity, i. e., the parity of the nucleon.

Several interesting phenomena have been observed at energies above the (3, 3) resonance (see Fig. 1). In the total cross section for π^- -p scattering there are two definite peaks; one is near 600 MeV and the other is near 900 MeV. For π^+ -p scattering there is a broad peak in the total cross section near 1350 MeV, and also a "shoulder" near 850 MeV.



MUB-1353

Fig. 1. Total cross sections for $\pi^\pm - p$ scattering, showing the energies at which differential cross sections were measured in this experiment.

It is possible that some of the peaks are elastic resonances superimposed on a normal elastic plus inelastic background, and that others are merely the result of a rapidly rising inelastic cross section which suddenly reaches the limit imposed on it by the unitarity condition at the energy of the peak. The last mechanism is discussed in more detail in reference 4.

Regardless of how the peaks are produced, it is desirable to learn as much as possible about them. At present there are no theories that correctly predict cross sections in this energy region. It is hoped that the data from this experiment will be an aid in the formulation of a theory which not only will correctly predict cross sections, but will also explain the nature of strong interactions in general.

Since all strong interactions are interrelated, a thorough knowledge of pion-proton interactions will be very helpful in explaining the various phenomena that occur in other types of strong interactions, such as the K meson-proton interactions, and the pion-hyperon interactions.

It is reasonable to hope that all strong interactions may someday be explained in terms of just a few basic interactions, such as the $(3, 3)$ resonance, the various π - π resonances, etc. Some of the π - π resonances are the ρ meson, a $T = 1$, $J = 1$, metastable "particle" of mass $M = 750$ MeV, which decays into two pions; the ω meson, a $T = 0$, $J = 1$, three-pion resonance "particle" of mass $M = 780$ MeV; and the η meson, a $T = 0$, $J = 0$, "particle" of mass $M = 550$ MeV.

At the present time it is conventional to characterize π -p scattering in terms of phase shifts, which are discussed in Sec. V. However, with only differential- and total-cross-section data it is extremely difficult, if not impossible, to determine uniquely all of the necessary scattering phase shifts. The reason for the difficulty is that numerous orbital angular-momentum states participate in the scattering in the energy region of this experiment; hence, it is necessary to determine a large number of phase shifts. In addition, these phase shifts are complex quantities, because inelastic scattering is allowed at these energies. In order to make a complete phase-shift analysis it is necessary to obtain additional data from experiments such as the measurements

of the polarization of the recoil proton in π -p elastic collisions,⁵ the total and differential cross sections for charge-exchange scattering (π^- -p \rightarrow π^0 -n),⁶ pion photoproduction cross sections,⁷ etc.

In Sec. V qualitative arguments are presented for the assignment of quantum numbers to the state that is responsible for the 1350-MeV resonance. The "shoulder" near 850 MeV in π^+ -p scattering is also discussed.

Because total isotopic spin is conserved in strong interactions, it is desirable to examine pion-nucleon scattering in terms of states of well-defined isotopic spin, rather than in terms of definite charge states. In order to obtain the cross section for isotopic spin $T = 3/2$, we can use the π^+ -p cross section alone. A linear combination of the cross sections for π^+ -p and π^- -p scattering (including charge exchange) may be used to calculate the $T = 1/2$ cross section. In this report the $T = 3/2$ (π^+ -p) scattering is examined.

II. EXPERIMENTAL METHOD AND EQUIPMENT

A. Experimental Method

A beam of positive pions of selected momentum was focused with small angular divergence on a liquid-hydrogen (LH_2) target. Then the differential cross sections for the elastic scattering of the pions was measured by detecting the scattered pion and the recoil proton in the proper time relationship with the incident pion. Scintillation counters were used as detectors.

The detection of inelastic scattering events in the elastic-scattering channels was minimized by the geometrical restrictions of the pion and proton counters. This method was used rather than one involving Cerenkov counters, or range telescopes, etc., because it accomplished its purpose adequately and it avoided the difficult corrections due to Cerenkov-counter inefficiencies or scattering in the range telescope, which must be applied when using the other methods. A measure of the inelastic scattering was made in order to correct the elastic data for inelastic events--this is explained in more detail in Sec. III B. Other corrections to the data are also discussed in Sec. III B.

Differential cross sections at laboratory scattering angles smaller than about 20 deg could not be measured, because for those events the recoil proton did not have enough energy to reach the proton counter and be counted.

The advantage of using a scintillation-counter array around the LH_2 target is that it is possible to obtain much better statistics in a shorter interval of time, as compared with methods using bubble chambers, spark chambers, etc. The statistics in this experiment averaged about 3 to 4%.

Figure 1 shows the total cross sections for π -p scattering, with vertical lines at those pion laboratory kinetic energies at which this experiment was performed: 533, 581, 698, 873, 990, 1311, and 1555 MeV.

Scattering from the empty hydrogen target was measured so as to correct for extraneous scattering from material in the beam, other than liquid hydrogen.

The pions incident on the liquid-hydrogen target were counted by using a monitor telescope consisting of three scintillation counters. The positions of these three counters are shown in Fig. 2, which is a plan view of the experiment. The number of monitor counts was corrected for muon-electron contamination in the beam, as measured by a gas Cerenkov counter.

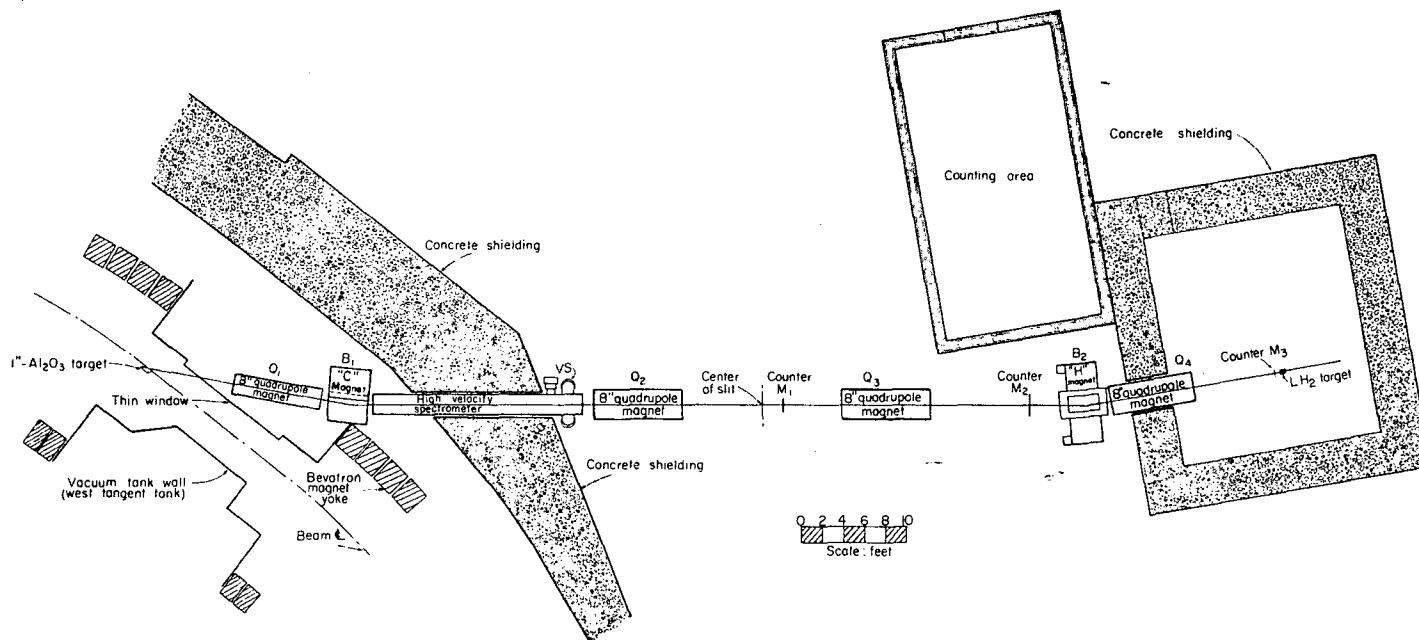
B. Equipment

1. Source of Pions

The pions were produced when an aluminum oxide ceramic target was struck by protons in the circulating beam in the Bevatron. The target was specially made to have a higher relative density (≈ 4) than most aluminum oxide ceramics. The number of pions produced in such a target is nearly proportional to the number of nucleons that are effective in contributing pion-producing collisions, per cm^3 of target. The total number of nucleons per cm^3 is $n = N_0 \rho$, where N_0 is Avogadro's number and ρ is the density of the target material. Since some of the nucleons in an atom of target material are "shadowed" by other nucleons, the equation for the effective density of nucleons becomes

$$n_{\text{eff}} = N_0 \rho \frac{A^{2/3}}{A} = N_0 \frac{\rho}{A^{1/3}},$$

where A is the total number of nucleons in each target atom. Therefore, in order to maximize the pion flux, it is necessary to maximize $\rho/A^{1/3}$. Positive and negative electrons are produced in the target when a neutral pion decays into photons and the photons create electron pairs. In order to minimize the electron contamination in the pion beam, it is necessary to minimize the conversion of the photons into



MUR 1230

Fig. 2. Plan view of the experimental arrangement. The counters, the LH_2 target, and the Al_2O_3 target are not drawn to scale.

electrons. This conversion rate is proportional to Z^2 , i. e. the square of the charge of each target nucleus. For this reason it is desirable to have a target with low Z . A ceramic target was chosen as a compromise between these two requirements.

When viewed in the direction of the secondary beam of pions, the target was 1/2 in. wide by 1/8 in. high. Some of the pions produced in the ceramic target were "collected" by an 8-in. -bore quadrupole placed at a 28-deg angle from the primary beam of protons. Because the 1/2-in. -wide ceramic target was also placed at a 28-deg angle with respect to the proton beam, it had an effective length of about 1 in. along the proton beam.

Approximately 10^{11} protons were "spilled" onto the ceramic target during each Bevatron pulse, thus producing approximately 20 000 pion counts per pulse in the monitor system. The pions were distributed as uniformly as possible over a time interval of 200 msec. The pion pulse was produced every 5 to 6 sec during the experiment.

2. Beam Design

The overall beam layout is shown in Fig. 2. The pions were transported from the Bevatron target to the liquid-hydrogen target by means of an optical system, shown schematically (not to scale) in Fig. 3. The optical system consisted of four 8-in. -bore quadrupoles, two bending magnets, a velocity spectrometer, and a copper slit. The primary purpose of the quadrupoles was to focus the pion beam on the hydrogen target, and also to produce an intermediate focus. The bending magnets determined the central momentum of the pion beam and, along with the copper slit, determined the momentum spread of the beam. The velocity spectrometer deflected protons out of the pion beam. The protons that were deflected a sufficient amount by the spectrometer collided with the copper slit and therefore did not reach the liquid-hydrogen target.

The four quadrupoles are designated as Q_1 , Q_2 , Q_3 , and Q_4 (listed from the Bevatron target to the liquid-hydrogen target). All of these quadrupoles were triplet quadrupoles, convergent in the end sections and divergent in the center section (CDC) in the horizontal plane.

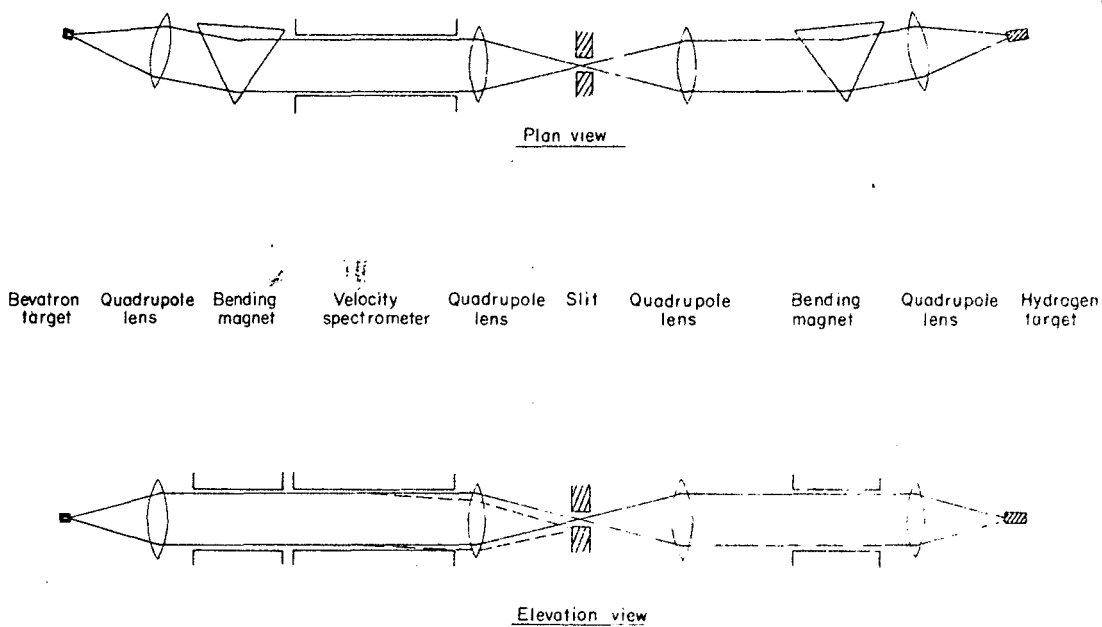


Fig. 3. Schematic diagram of optical system showing extreme rays of pion beam, various magnets, targets, slit, and velocity spectrometer. The dashed lines illustrate how the protons were stopped by the slit.

Each quadrupole was placed such that its pole face at one end was 104 in. from either a focal point in the beam or the Bevatron target. All quadrupoles rendered (or received) the beam nearly parallel in both planes at their other end. In the case of Q_1 and Q_4 , the beam was not quite parallel in the vertical plane—in order to compensate for a slight vertical focusing by the bending magnets B_1 and B_2 . Although Q_1 subtended a solid angle of approximately 4 msr from the Bevatron target, the effective solid angle was only about $2\frac{1}{2}$ msr, because approximately 40% of the pions that entered Q_1 could not enter the velocity spectrometer VS. The reason for this was that the horizontal plates in VS were only 4 in. apart, rather than 8 in., the diameter of the bore of Q_1 .

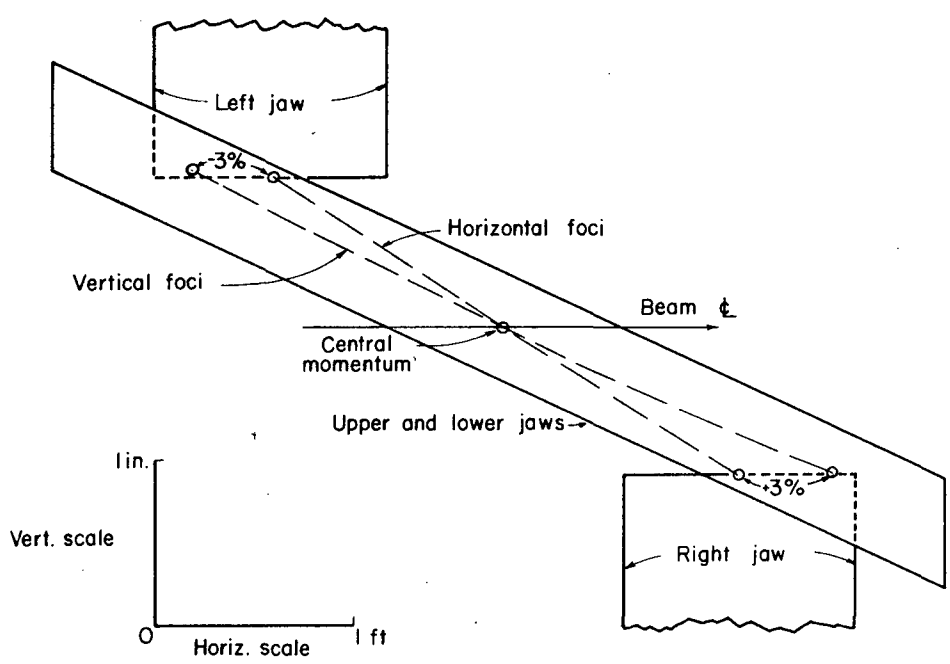
The first bending magnet, B_1 , was a 16- by 36-in. C-magnet with a 6-in. gap. A C-magnet was used in order to keep the pion beam as close to the Bevatron as possible and thereby minimize the "takeoff" angle (28 deg) of the pions. The pion flux increases as the takeoff angle is decreased. Because of its proximity to the Bevatron, the magnetic field in B_1 tended to fluctuate ($\Delta H/H \approx \pm 0.6\%$) in phase with the Bevatron's varying magnetic field. This problem was overcome by incorporating a voltage feedback circuit into B_1 . A search coil was used in B_1 to verify that the feedback circuit actually stabilized the magnetic field in B_1 ($\Delta H/H \approx \pm 0.16\%$). The pion beam was bent 10 deg in B_1 and another 10 deg in the same direction in B_2 .

The various momenta in the pion beam were dispersed by B_1 , a momentum band of $\pm 3\%$ was selected by a copper slit at the intermediate focus, and then these momenta were nearly recombined by B_2 , an 18- by 36-in. H-magnet with a 6-in. gap. It was B_2 that "defined" the central momentum at which each set of data was taken. Bending magnet B_2 was carefully "wire-orbited" (floating-wire technique) three times prior to the collection of data, in order that the field strength needed for each momentum would be accurately known. The three wire-orbit measurements agreed very well with each other. In order to adjust the rest of the optical system so as to get a maximum pion flux, a computer program, OPTIK,⁸ was used to calculate the field

strengths in all of the components of the optical system, in relation to a given field in B_2 . Upon completion of the experiment, an elaborate study was made of the values of the momenta of the experiment. They are now known to an accuracy of $\pm 1.1\%$. This momentum determination is discussed in Appendix A.

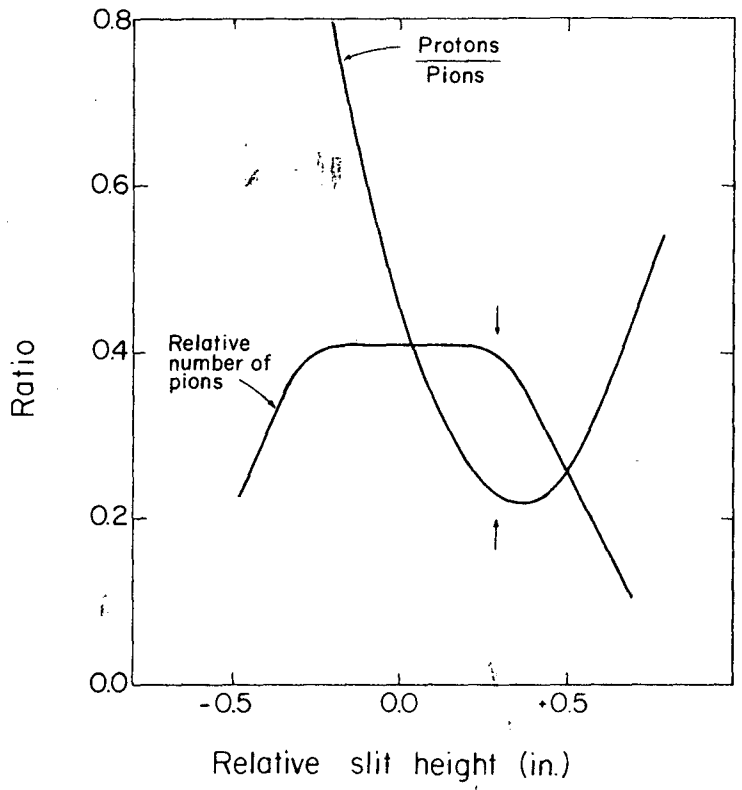
In addition to determining the width of the momentum band used in the experiment, the copper slit also served to stop protons that were deflected downward by the velocity spectrometer. The copper slit is shown in Fig. 4. For the sake of clarity, the vertical scale is ten times as large as the horizontal scale. The slit was designed so that the copper was always positioned above and below the locus of the vertical focal points of the various momenta. Figure 4 shows the specific points where the central momentum, +3% momentum, and -3% momentum are focused; as well as the locus of the focal points in both the vertical and horizontal planes. Notice that the +3% and -3% momenta have their horizontal focal points at the centers of the faces of the side jaws of the slit. Therefore, one side jaw was positioned about 28 in. "downstream" from the other side jaw. The effective length of the copper along the beam was 14 in. for all parts of the slit. The slit was set on several inches of lead, which stopped those protons that were deflected below the slit by the spectrometer. The height of the copper slit and the lead was adjustable so as to vary the number of protons and the number of pions that were stopped by the slit. Figure 5 shows both the relative number of pions and the ratio of protons to pions plotted vs slit height. The arrows indicate the position of the slit at which data were taken at this energy (873 MeV). The slit was made of copper, because it has such a high stopping power for protons per unit length of material.

The velocity spectrometer was designed to deflect protons downward, and yet leave the pions nearly undeflected, by means of a vertical electric field and a horizontal magnetic field. Figure 6 shows a cross-sectional view, looking downstream along the pion beam, of the spectrometer, including the electric field vector \vec{E} and the magnetic field vector \vec{B} . Since the force due to the electric field is $\vec{F}_E = q\vec{E}$, where q is the charge of the particle, this force is the same for both the pion



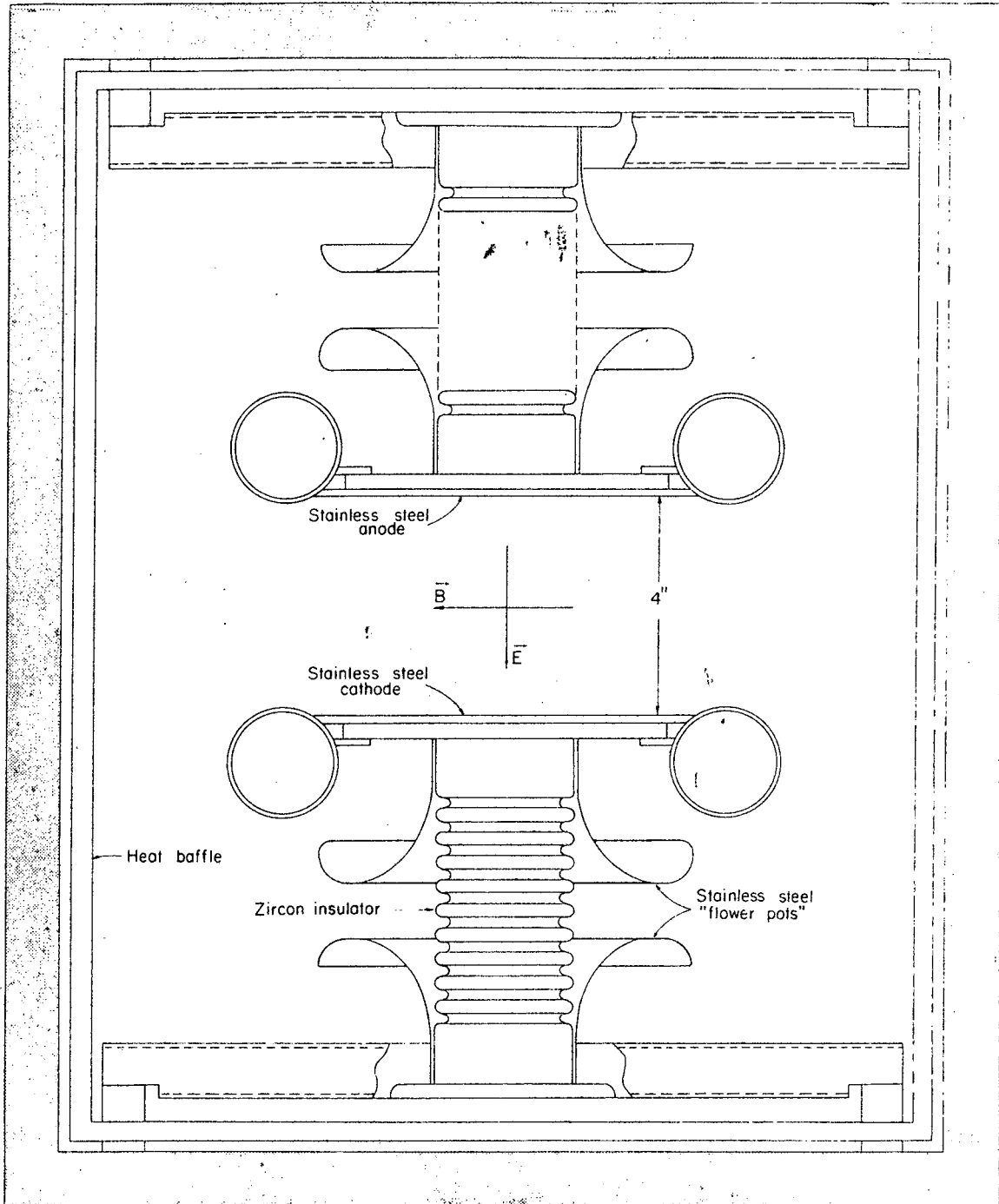
MU-27620

Fig. 4. Copper slit. The pion-beam focal points in the vertical and horizontal planes for the central momentum, +3% and -3% momentum are also shown.



MU-27619

Fig. 5. Curves showing ratio of protons to pions (before protons were eliminated by time of flight), and relative number of pions plotted vs slit height for an incident pion lab kinetic energy of 873 MeV.



MUR 1239

Fig. 6. Cross-sectional view of velocity spectrometer showing direction of electric and magnetic fields as viewed looking downstream along the pion beam.

and the proton, and is in a downward direction. The force due to the magnetic field is $\vec{F}_B = q(\vec{v}/c) \times \vec{B}$, where \vec{v} is the velocity of the particle and c is the velocity of light in a vacuum. Although the pion and proton both have the same momentum, they have different velocities, and hence the upward force due to the magnetic field is different for the pion and the proton. For example, if the momentum is 1000 MeV/c, v/c for the pion is 0.99, whereas v/c for the proton is 0.73. Therefore the upward force on the proton is only about 3/4 as large as the upward force on the pion. By adjusting the magnetic and electric fields such that the force on the pion due to the magnetic field is equal and opposite to the force due to the electric field, the pions will be undeflected, but the protons of the same momentum will be deflected in the direction of the electric field. Equations relating to the amount of deflection of the protons are presented in Appendix B. By using the velocity spectrometer the ratio of protons to pions at 1555 MeV was reduced from ≈ 15 to ≈ 3 . At 533 MeV the final proton-to-pion ratio was 0.02. Those protons that physically got through the monitor telescope were eliminated by "time-of-flight." (This system is discussed in Sec. IIB5.)

The spectrometer used in this experiment was 20 ft long. The distance between the electric plates was 4 in., and the voltage across them was usually 450 kV. At the lower pion energies the voltage was sometimes reduced to 400 kV, and at other times the voltage was raised to nearly 500 kV. In order to maintain such a high voltage across the plates, it was obviously necessary to put the electric plates in a vacuum. Actually, it was easier to maintain the high voltage by flowing argon through the spectrometer at a pressure of about 1 μ . This near-vacuum was extended upstream through B_1 and Q_1 , so there was very little air in the beam line between the Bevatron target and the downstream end of the spectrometer. From this point to the liquid-hydrogen target, helium bags were put in the beam line to exclude the air, and hence reduce the scattering of the pions on air molecules. The helium bags were about 9 in. in diameter and about 20 ft long.

The velocity spectrometer (VS) was shielded from the magnetic field of the Bevatron by a 3- by 5-ft by 10-in. piece of iron inserted

between the Bevatron yoke and that end of VS nearest to the Bevatron. Quadrupole Q_1 was shielded by placing it inside an open-ended iron box with $1\frac{1}{2}$ -in. -thick walls.

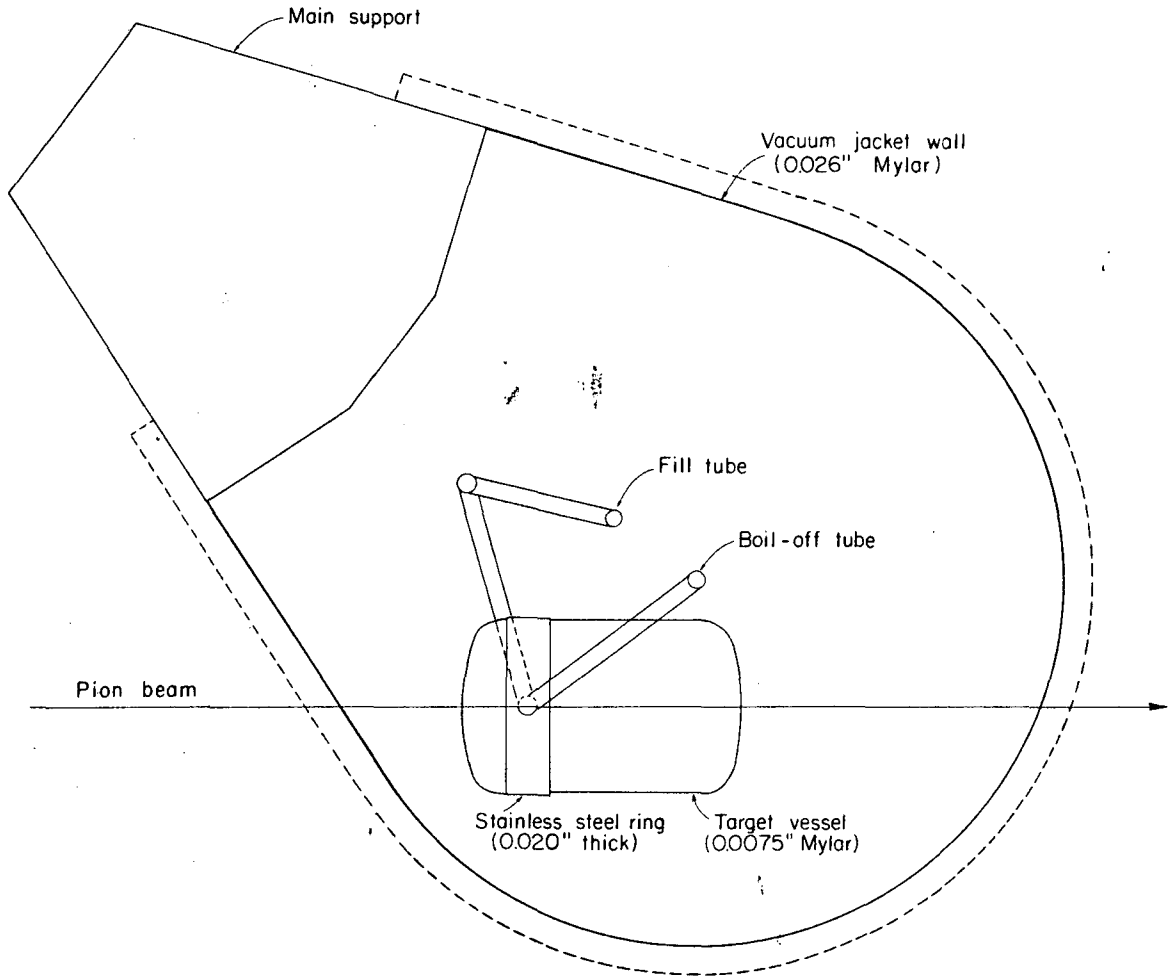
All of the beam components were carefully surveyed into place, and were positioned within $1/16$ in. of their correct positions.

3. Liquid-Hydrogen Target

The liquid-hydrogen target used in the experiment is shown in Fig. 7. The target vessel was a Mylar cylinder $2\frac{1}{2}$ in. in diameter and 4 in. long. The vessel was enclosed in a vacuum and surrounded by radiation shields of aluminized Mylar to minimize heat transfer to the liquid hydrogen. The target vessel was filled by gravity feed from a reservoir above it. The liquid-hydrogen reservoir was surrounded by a liquid-nitrogen jacket, and the entire assembly was enclosed in a vacuum jacket. The target vessel was emptied by closing its boil-off valve, thereby building up a slight gas pressure in the target and forcing the liquid hydrogen out the bottom. The density of the gaseous hydrogen left in the target⁹ was 0.00136 g/cm^3 , whereas the density of the liquid hydrogen is only 0.0702 g/cm^3 ; this required a 2% correction to be applied to the amount of liquid hydrogen.

The effective number of protons per cm^2 , nx , was calculated to be 4.196×10^{23} . This value includes the 2% density correction, and takes into consideration the shape of the target vessel, and the beam profile (relative intensity of the pion beam for positions off the central beam axis).

The hydrogen target was designed so as to minimize the number of supports and other obstacles between the target vessel and the scintillation-counter arrays (see Fig. 7). The $5/8$ -in. -wide 0.020 -in. -thick stainless steel band was used to attach the fill tube at the bottom of the target vessel, and the boil-off tube at the top. The various thicknesses of Mylar used to contain the hydrogen and the vacuum around the target vessel are shown in Fig. 7!



MUR-1238

Fig. 7. Plan view of liquid-hydrogen target vessel and surrounding vacuum-jacket wall.

The various gauges and operating controls associated with the hydrogen target were located in the counting area, so it was not necessary to go into the actual target area very often.

4. Scintillation Counters

Figure 8 shows the entire counter array schematically. Three counters (M_1 , M_2 , and M_3) were used to count those pions, incident on the liquid-hydrogen target, that could contribute to the scattering data. There were 21 counters, labeled π counters, placed at various laboratory angles between 16 and 145 deg to the right of the beam, as viewed looking downstream. The purpose of these counters was to detect the scattered pions. Twenty-five counters, labeled ρ counters, were placed to the left of the beam at laboratory angles between 4 and 82 deg. These counters detected the protons as they recoiled from the π -p elastic collisions. The ρ counters were added together electronically in overlapping groups of three to six counters. These groups of ρ counters were called P counters. For each π counter there was a corresponding P counter. The P counter was very slightly larger than necessary to detect the proton recoiling from any elastically scattered pion that was detected in the corresponding π counter.

All of the counters used in this experiment, except the gas Cerenkov counter, were scintillation-type counters made of a solid solution of terphenyl in polystyrene plastic. Photons, produced when a charged particle passed through one of the scintillators, were transmitted through a lucite light pipe to a 6810A photomultiplier tube, where the light pulse was converted to an electrical pulse. High-capacitance tube bases were used on all counters. Those in or near the pion beam required extra-high-capacitance bases, because of their high singles counting rate.

Counter M_1 was located at the downstream end of the slit, and was 4.5 in. wide, 2.5 in. high, and 0.25 in. thick. Counter M_3 was located directly in front of the liquid-hydrogen target vessel; i. e., upstream from the target. This counter was a 1/8 in. -thick disk,

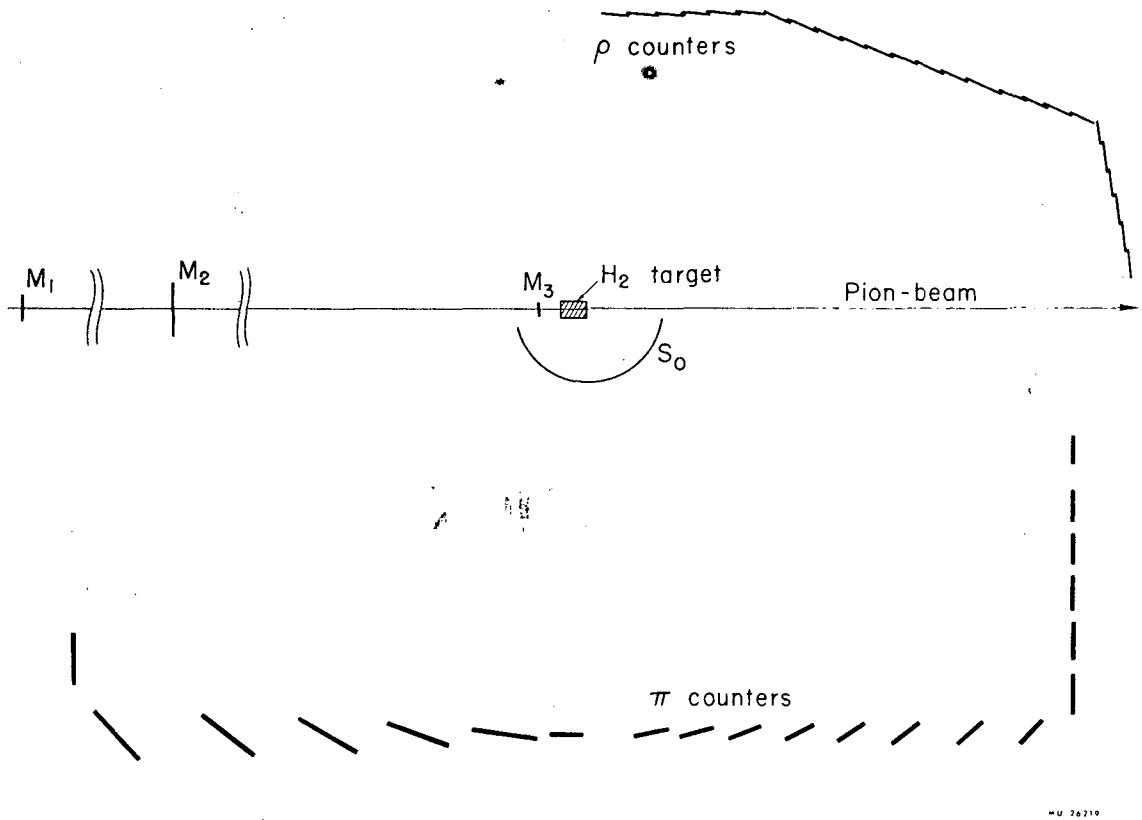


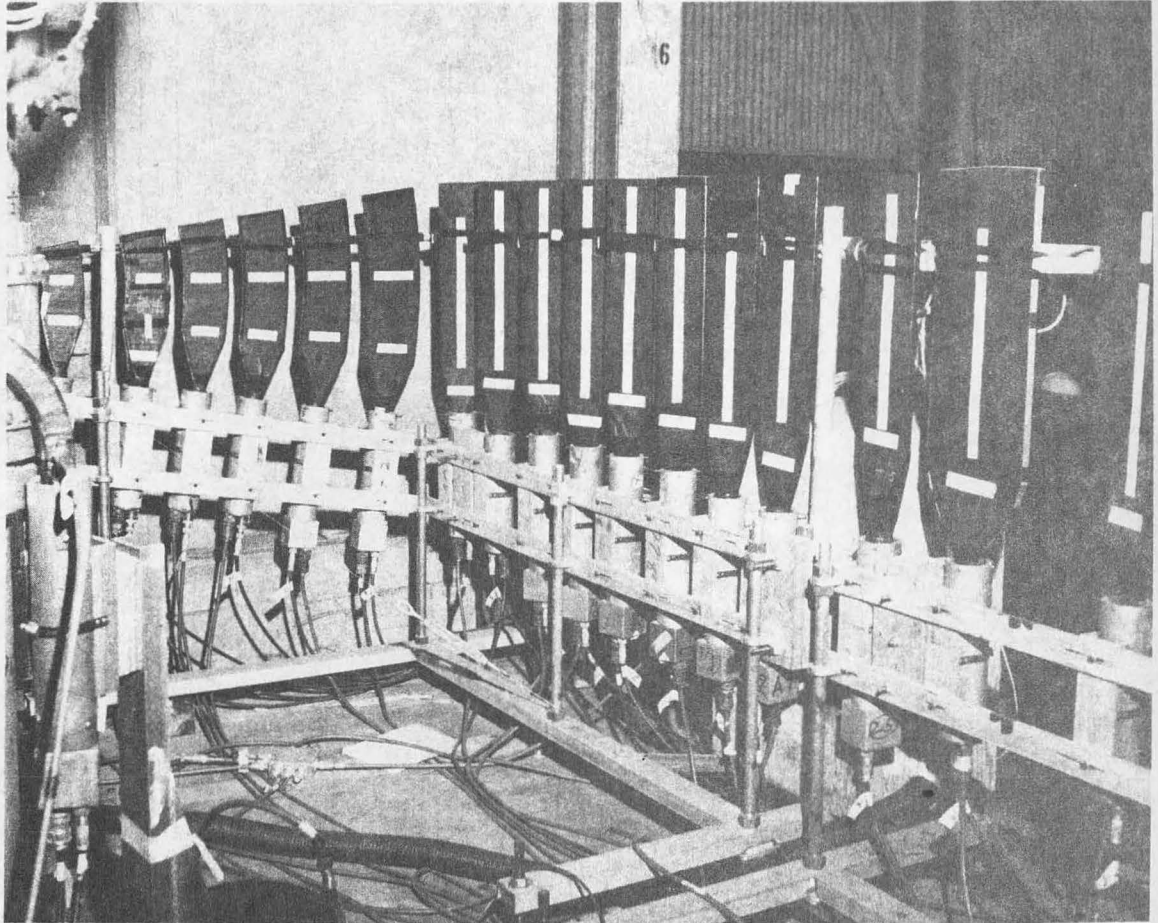
Fig. 8. Plan view of scintillation-counter arrangement.

1.5 in. in diameter. Since M_3 was smaller than the target vessel, it served to define the beam diameter at the target. Counter M_3 , along with Q_4 , limited the amount of beam convergence at the hydrogen target to ± 1.5 deg. Counter M_3 is also shown in Figs. 9 and 10. The distance between M_1 and M_3 was approximately 47 ft. Counter M_2 was located halfway between M_1 and M_3 , and was rectangular in shape, 0.25 in. thick by 6 in. high by 8.5 in. wide. Counters M_1 and M_2 were both large enough to detect all of the particles in the beam.

The π counters, which detected scattered pions, were all designed to subtend an angle of 18 deg in ϕ , the azimuthal angle in a spherical-coordinate system. Table I lists the angles at which each π counter was placed, the counter width, and the solid angle it subtended. The angles and solid angles are given in the lab system. The solid angles and the cosines of the pion scattering angles, both in the c.m. system, are listed in Tables II(a) and II(b), respectively, for each energy.

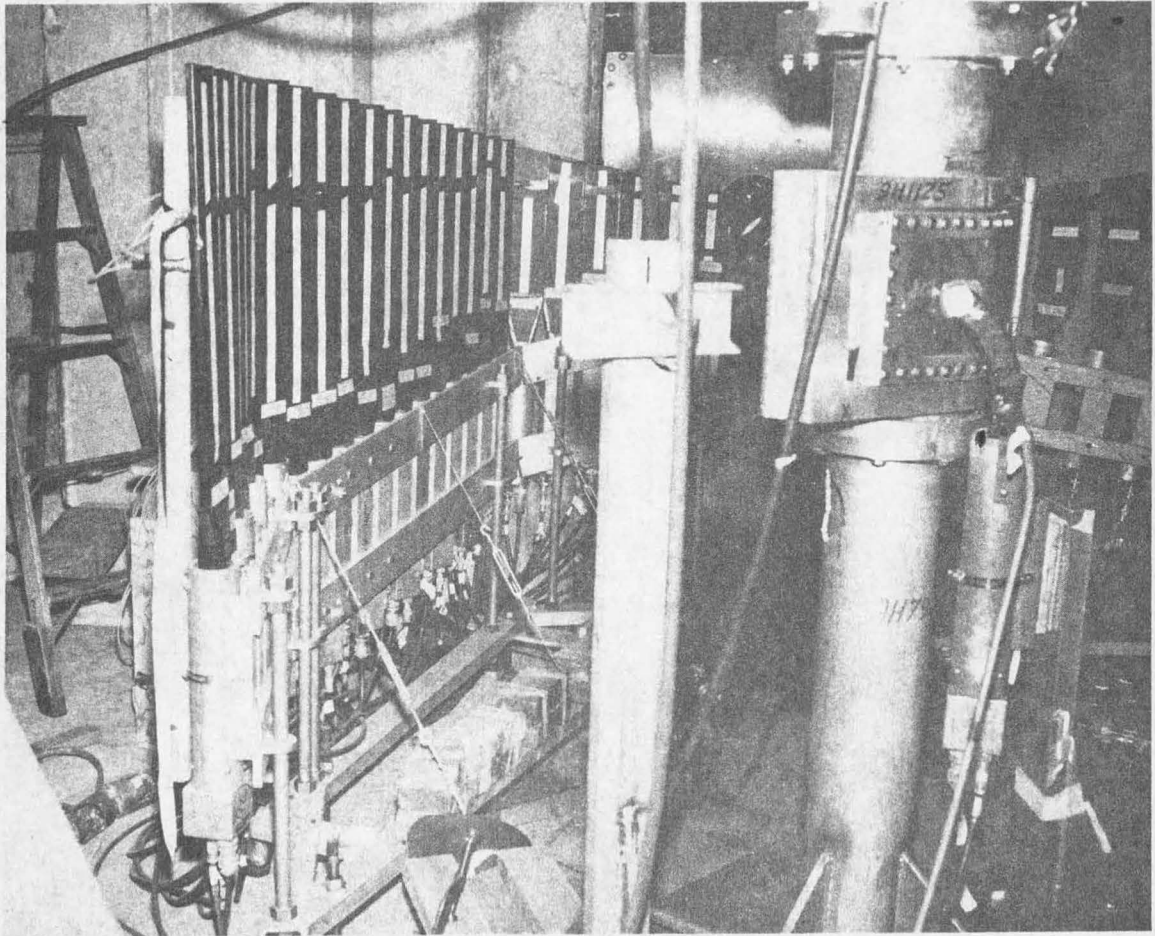
The 25 ρ counters, which detected the recoil protons, were all $3/8$ in. thick and 4 in. wide. Most of them were rectangular, some being as long as 22 in. The ρ counters were all designed to subtend an angle $\phi \approx 22$ deg, so that the ρ counters that were closer to the pion beam were shorter in length. In the extreme cases where the ρ counters were placed at smaller angles to the beam, the side of the ρ counter that was closer to the beam was shorter than the other side, so these ρ counters were trapezoidal in shape. The shortest side of the shortest ρ counter was 4.2 in. long.

Figure 9 is a photograph showing most of the π counters, and M_3 with its curved light pipe. Figure 10 shows the ρ counters and the outside of the LH_2 target vacuum jacket with M_3 in front. Figure 11 is an overall view of the experimental area, showing the backs of the π counters, the downstream end of Q_4 on the left, and the upper portion of the LH_2 target in the center. Those π counters directly in front of the hydrogen target in Fig. 11 have 0.5 in. -thick rectangular scintillators that are 10 in. wide and 20 in. high. These counters have a



ZN-3310

Fig. 9. Some of the π counters.



ZN-3309

Fig. 10. Liquid-hydrogen target with ρ counters on left.

Table I. Pion-counter data: lab angles

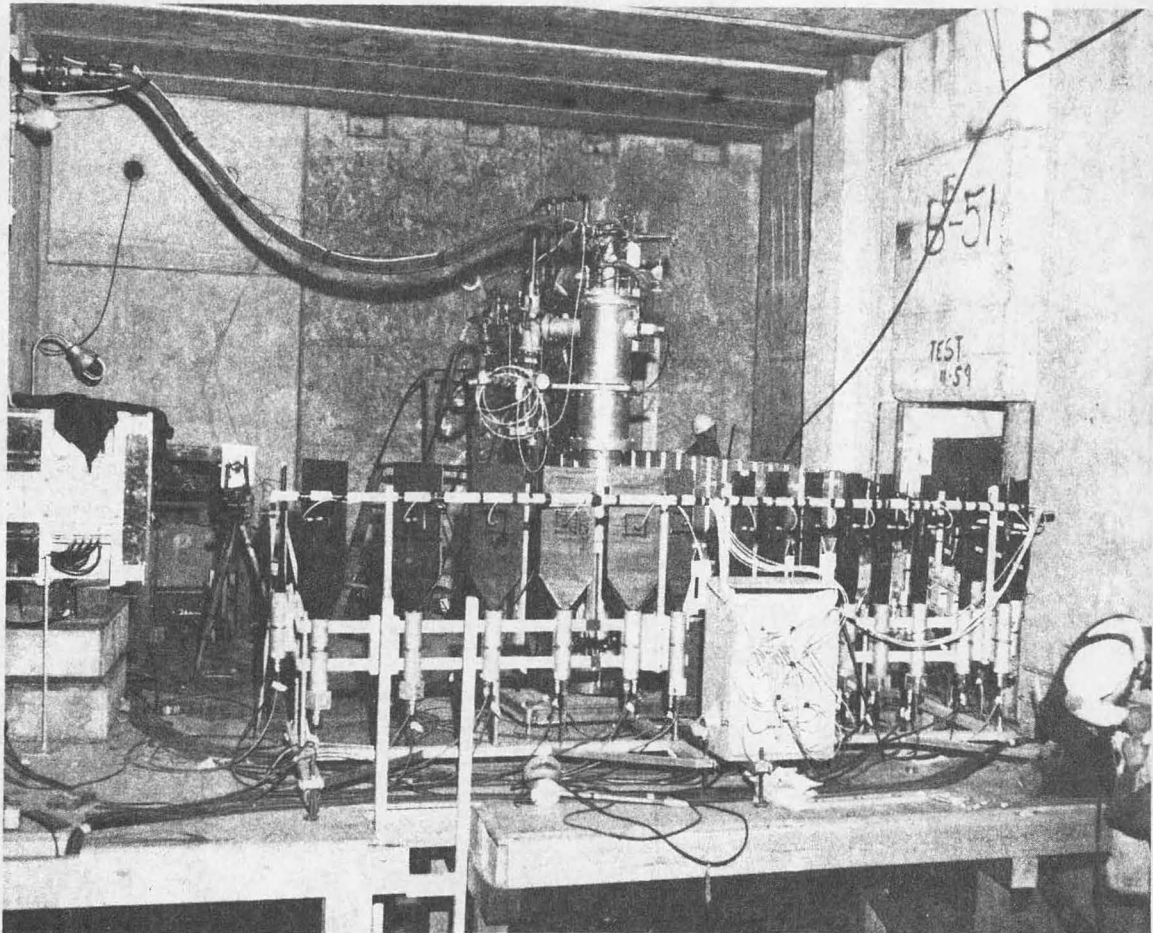
Counter number	Angle of scatter (deg)	Counter width (in)	Solid angle (msr)
1	16	4.20	4.534
2	22	4.52	6.161
3	26	4.81	7.210
4	30	5.19	8.224
5	34	5.66	9.197
6	38	6.27	10.126
7	43	5.00	11.492
8	47	5.00	13.195
9	52	5.00	15.401
10	57	5.00	17.467
11	62	5.00	19.327
12	68	5.00	21.538
13	74	5.00	23.112
14	80	5.00	23.918
15	91	5.00	25.208
16	99	10.00	48.751
17	110	10.00	43.783
18	120	10.00	37.349
19	129	10.00	30.012
20	137	10.00	23.143
21	145	7.69	12.578

Table II(a). Pion solid angles, c. m. system.

Counter number	Solid angles (msr)						
	Incident pion lab kinetic energy (MeV)						
	533	581	698	873	990	1311	1555
1	10.546	10.949	11.902	13.298	14.207	16.620	18.365
2	13.684	14.160	15.273	16.871	17.889	20.509	22.329
3	15.417	15.912	17.058	18.674	19.685	22.220	23.922
4	16.846	17.337	18.460	20.010	20.960	23.267	24.754
5	17.967	18.433	19.485	20.901	21.747	23.726	24.935
6	18.789	19.213	20.156	21.387	22.100	23.688	24.593
7	19.898	20.262	21.048	22.025	22.562	23.658	24.195
8	21.550	21.867	22.535	23.321	23.725	24.452	24.720
9	23.305	23.546	24.026	24.525	24.739	24.974	24.905
10	24.426	24.574	24.831	25.012	25.027	24.773	24.392
11	24.934	24.980	25.004	24.867	24.692	23.997	23.352
12	25.198	25.123	24.877	24.387	24.009	22.865	21.969
13	24.520	24.336	23.856	23.076	22.540	21.078	20.025
14	23.037	22.767	22.110	21.128	20.491	18.850	17.730
15	20.459	20.079	19.206	17.999	17.261	15.480	14.340
16	35.184	34.381	32.576	30.166	28.733	25.381	23.301
17	27.234	26.478	24.816	22.667	21.425	18.606	16.913
18	20.604	19.956	18.553	16.778	15.770	13.530	12.213
19	15.065	14.551	13.449	12.075	11.304	9.614	8.635
20	10.808	10.418	9.588	8.564	7.994	6.757	6.048
21	5.528	5.320	4.879	4.340	4.042	3.400	3.035

Table II(b). Cosines of pion scattering angles, c. m. system.

Counter number	$\text{Cos } \theta^*$						
	Incident pion laboratory kinetic energy (MeV)						
	533	581	698	873	990	1311	1555
1	0.907	0.904	0.895	0.882	0.873	0.850	0.832
2	0.830	0.823	0.808	0.785	0.770	0.731	0.702
3	0.768	0.759	0.739	0.709	0.690	0.640	0.603
4	0.700	0.689	0.664	0.627	0.604	0.543	0.500
5	0.626	0.613	0.583	0.540	0.513	0.443	0.394
6	0.547	0.533	0.499	0.450	0.420	0.342	0.289
7	0.446	0.429	0.391	0.336	0.303	0.218	0.161
8	0.363	0.345	0.303	0.246	0.210	0.121	0.063
9	0.259	0.239	0.195	0.134	0.097	0.006	-0.053
10	0.155	0.135	0.089	0.027	-0.011	-0.101	-0.160
11	0.054	0.034	-0.013	-0.075	-0.112	-0.201	-0.257
12	-0.062	-0.083	-0.129	-0.190	-0.226	-0.310	-0.363
13	-0.173	-0.193	-0.237	-0.295	-0.329	-0.407	-0.456
14	-0.276	-0.295	-0.336	-0.391	-0.422	-0.494	-0.537
15	-0.445	-0.461	-0.497	-0.542	-0.568	-0.627	-0.662
16	-0.551	-0.565	-0.596	-0.635	-0.657	-0.705	-0.734
17	-0.675	-0.686	-0.710	-0.740	-0.756	-0.793	-0.814
18	-0.768	-0.776	-0.794	-0.816	-0.828	-0.855	-0.870
19	-0.836	-0.842	-0.855	-0.871	-0.880	-0.899	-0.910
20	-0.885	-0.890	-0.899	-0.910	-0.917	-0.930	-0.938
21	-0.925	-0.928	-0.934	-0.942	-0.946	-0.955	-0.960



ZN-3308

Fig. 11. Overall view of counter arrangement showing backs of π counters.

tapered light pipe and shielded phototube at the bottom. In order to shield the counters from some of the external radiation, the walls of the experimental block house were 4-ft-thick concrete, and the roof was 2-ft-thick concrete.

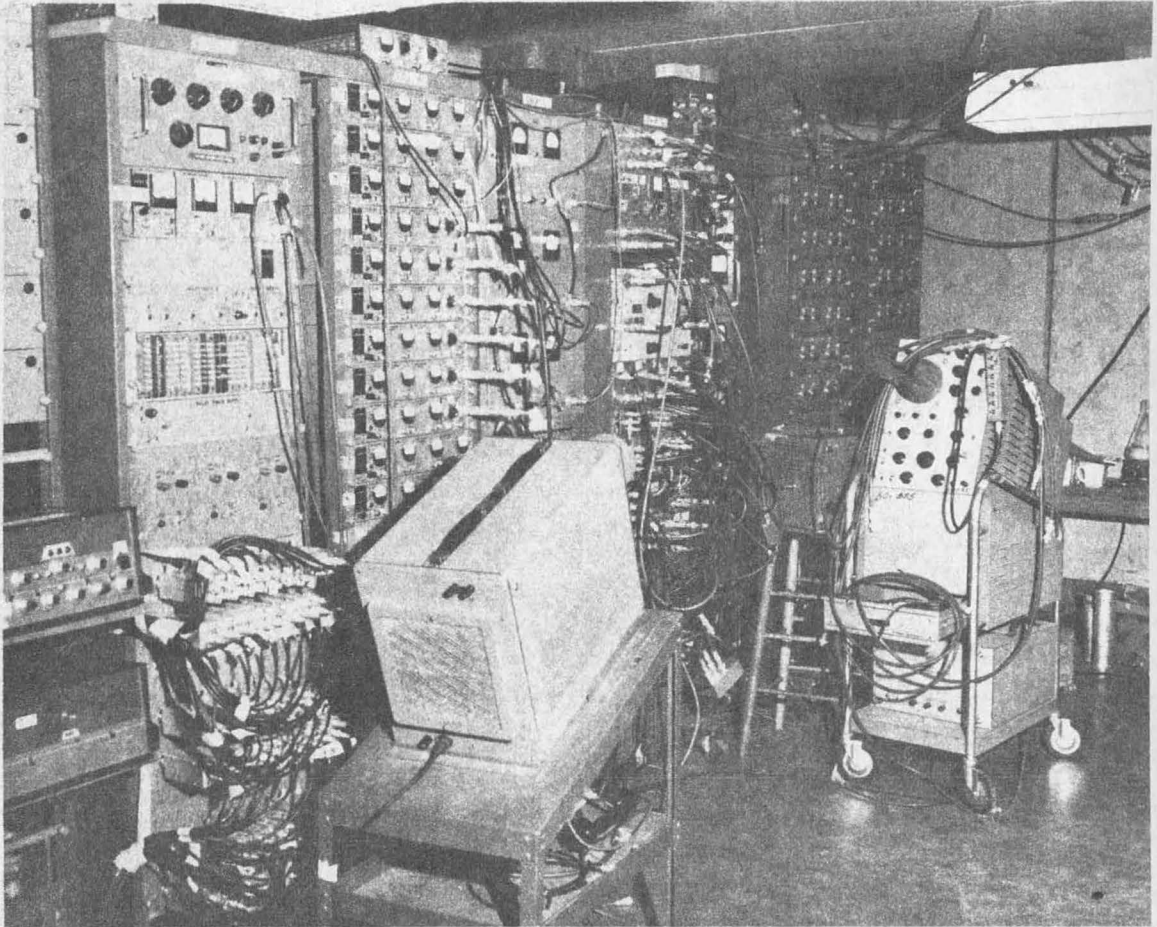
A special counter, S_0 , was used in this experiment (shown schematically in Fig. 8). Its use is described in the next section. A straight line from any point in the liquid-hydrogen target to any point on any π counter would pass through the S_0 counter. Pions in the main beam that were not scattered by the LH_2 target missed the S_0 counter.

The gas Cerenkov counter is discussed in Sec. IIB6.

5. Electronics

Figure 12 is a photograph showing a portion of the electronics. Figure 13 is a schematic diagram of the electronics. Some of the elements in Fig. 13 are numbered from one to eight. This labeling system is explained in Table III. Most of the electronics used is described in either reference 10, 11, or 12.

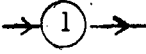
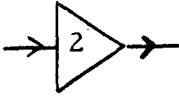
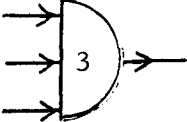
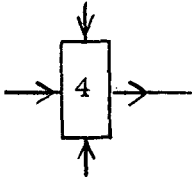
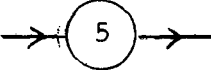
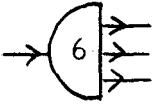
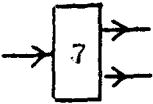
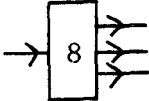
Two types of scattering events, elastic and inelastic, were measured in this experiment. The number of elastic events in the n th elastic channel was measured by counting coincidences between counter π_n , the corresponding P_n counter, and the monitor system, $M_1M_2M_3$. Inelastic events were measured as coincidences between counter π_n , a ρ counter which was not common to P_n , and the monitor system. The signal from the P_n counter was inverted and called \bar{P}_n . This \bar{P}_n signal was added to the coincidences measuring inelastic events so as to put the P_n counter in anti-coincidence with the rest of the counters. The reason for this was to discard any inelastic events associated with counter π_n that occurred simultaneously with a coincidence in the n th elastic channel. This was done because the storage system could only store one event at a time. This is discussed in more detail below. The ρ counter that was put in coincidence with the π_n counter to measure inelastics was labeled I_n so as to facilitate renumbering. Actually there were two inelastic channels for each π_n counter, and the corresponding two ρ counters were labeled I_{nA} and I_{nB} .

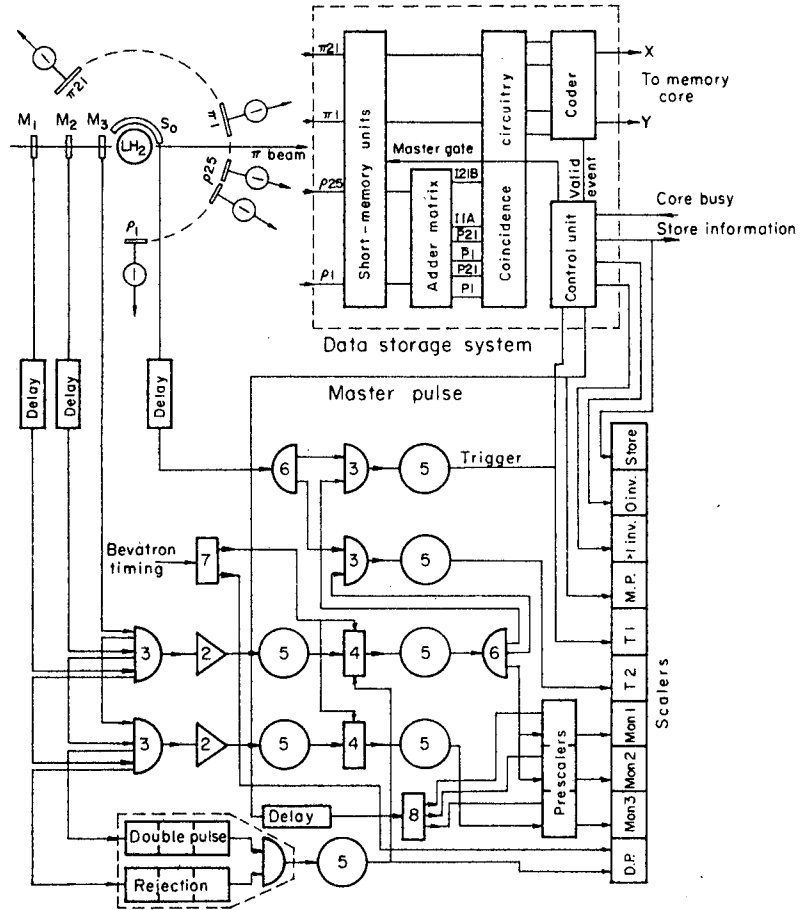


ZN-3311

Fig. 12. A portion of the electronics.

Table III. Symbols used in Fig. 13 and their explanation.

Symbol	Description
	Tunnel-diode pulse discriminator and shaper.
	Fast amplifier, Hewlett-Packard 460B.
	Fast coincidence circuit, Lawrence Radiation Laboratory Wenzel tube.
	Gate circuit, turned off by + 2V input.
	Pulse-amplitude discriminator, Lawrence Radiation Laboratory Model III Jackson.
	Pulse splitter.
	Lawrence Radiation Laboratory scalar gate and beam monitor with modified output.
	Special gate circuit used to turn off prescalars during time data storage system is busy.



MU.27660

Fig. 13. Block diagram of electronics.

There were three main sections of electronics: the monitor section, the matrix coincidence system, and the storage section. The monitor section measured coincidences between counters M_1 , M_2 , and M_3 , and coincidences between the S_0 counter and the output of the first coincidence. The output from the latter coincidence was used to trigger the matrix coincidence system. The coincidences for the 21 elastic channels and the 42 inelastic channels were formed in the matrix coincidence system. The output from the 63 channels of the matrix coincidence system were fed to the magnetic-core storage of a pulse-height analyzer. This represented the storage section.

The pulses from the monitor counters M_1 , M_2 , and M_3 were synchronized at the coincidence circuit by using pions in the pion beam. The phototube voltages were also adjusted while the counters were in the beam, by observing the output pulses on a Tektronix 517A cathode-ray oscilloscope.¹⁰ The voltage was increased until the output pulse was large enough, i. e., -3V, to reliably operate the tube-type Wenzel coincidence circuit.¹² Since not all of the protons in the pion beam were eliminated by the velocity spectrometer and the copper slit, the rest of them were eliminated electronically by time-of-flight. If a pion and a proton of the same momentum passed through M_1 together, the proton would reach M_3 at least 7 nsec after the pion. Seven nanoseconds corresponds to the delay time for the highest experimental energy. At lower energies this time difference would be even greater. The monitor coincidence circuit had a resolution time of 2 nsec and was timed for pions; hence, the protons reached M_3 at least 7 nsec too late to be counted reliably. Less than 0.1% of the total monitor counts resulted from protons.

If two charged particles traversed the beam line with less than a 40-nsec time separation, a double-pulse-rejection system was activated, and the pulses from both particles were rejected. That is, they neither counted in the monitor system nor triggered the rest of the electronics. Consequently, in order for a pion to count in the monitor system it not only had to travel from M_1 to M_3 within about 2 nsec of the correct time, but it also could not be followed or preceded by another charged

particle within a 40-nsec time interval. There were three reasons for using this double-pulse-rejection system. First, it was imperative that there was only one scattering event for each "cycle" of the matrix coincidence system. If more than one scattering event had been allowed in a cycle, the system would have tried to store both events simultaneously and, since this could not be done, both events would have been lost. However, the two particles would still have counted in the monitor system. The effective time for the pulses from any scattering event to enter the matrix coincidence system was the length of the gate to the matrix. This gate was 35 nsec long. A 40-nsec time resolution was chosen for the double-pulse-rejection system, so that it would be slightly longer than the gate to the matrix.

The second reason for using the double-pulse-rejection system was to keep the number of counts in the monitor system equal to the number of pions that had an opportunity to scatter. If, for example, two pions had been allowed to count as they simultaneously traversed the beam line, they would have produced only one count in the monitor system. However, the two pions together would have had twice the probability for scattering, even though one of the pions may have missed M_3 , but still had entered the hydrogen target. Because M_3 was smaller than the beam, the double-pulse-rejection system was activated by counters M_1 and M_2 only. Counters M_1 and M_2 were both large enough to detect all of the particles in the beam.

A third reason for using the double-pulse-rejection system was to reduce the number of accidental counts in the monitor system to a negligible amount. This is discussed in Sec. IIIB2.

Actually, all three of these reasons amount to maintaining a correct monitoring of the beam in relation to the data accepted by the matrix system.

As mentioned above, counters M_1 and M_2 were used to activate the double-pulse-rejection system. The pulses from each of these counters were "stretched" to about 45 nsec in length. If two pulses from one of the counters were within about 40 nsec of each other, they

would overlap a sufficient amount and result in a pulse with twice the amplitude. By feeding these pulses into a discriminator it was possible to determine if there was such an overlap of the pulses. The output of the discriminator associated with M_1 was put in coincidence with the discriminator output from M_2 . If the double-pulse occurred in both counters, this coincidence put out a pulse that was shaped and used as a gate for the output of the $M_1M_2M_3$ coincidence.

The output M from the $M_1M_2M_3$ coincidence was put in coincidence with the S_0 counter. The resolution time of this MS_0 coincidence was 20 nsec. The output T of the MS_0 coincidence used to trigger the coincidence matrix system. By using S_0 in this way the duty cycle of the matrix system was reduced by a factor of about 50 with respect to triggering on M alone. In order for pulses from the π and ρ counters to enter the matrix system, they had to occur within 35 nsec of the trigger T, which effectively was the gate to the matrix coincidence system. This gave a reasonable assurance that the π and ρ pulses were related to the beam particle that initiated the trigger. The gate to the matrix coincidence system was 35 nsec long because it was essentially a coincidence between two 35-nsec pulses. One of these pulses was generated by the trigger T, and the other came from one of the tunnel-diode limiters on one of the π or ρ counters. Once the π and ρ counter pulses entered the matrix system, they encountered coincidence circuits with long resolution times. The reliability of the system was thereby increased. At certain times, e. g., when the π and ρ pulses associated with a particular pulse from T were being checked for the proper coincidences, the matrix system was unable to accept any additional pulses. During these times the monitor prescalers and scalers were gated off, so that the correct relationship between the number of monitor counts and the rest of the data was maintained. This gate varied in length from 7 to 100 μ sec, depending upon how long the matrix system was busy. The average length of the gate was approximately 20 μ sec.

If only one of the 63 coincidences in the coincidence matrix system occurred for a given trigger, the event was stored in the magnetic cores of a pulse-height analyzer. If there was no coincidence for a given trigger, the trigger was counted in a scaler labeled "zero invalids." If there was more than one coincidence for a given trigger, the trigger was recorded in a scaler labeled "> 1 invalids," and the coincidences were not stored in the pulse-height analyzer. The > 1 invalids did not occur very frequently, and it is believed that essentially no elastic data were lost as a result of this type of invalid event. After an appropriate length of running time, the number of counts in each of the 63 channels was read out of the pulse-height analyzer by being both typed on an electric typewriter and punched onto IBM cards.

A test system was used to test all of the electronics as a unit. The test system used light pulsers attached to each counter. All possible π - ρ counter pairs were pulsed in a systematic manner, along with M_3 , S_0 , and another counter L, which replaced M_1 and M_2 in the monitor coincidence. Therefore, each time the light pulser was triggered, five counters received pulses. They were L, M_3 , S_0 , π_k , and ρ_ℓ , where k ranged from 1 to 21, and ℓ ranged from 1 to 25 for each value of k. It required 525 pulses to check all of the π and ρ counter pairs. Therefore, a complete check cycle required 525 pulses. The electronics was checked for malfunction by running the test system through N cycles, and then examining each of the 63 pulse-height analyzer outputs to see if it was the correct multiple of N. For convenience in reading the pulse-height analyzer outputs, the test system was usually operated for ten cycles.

The light-pulser system was used to time the π and ρ counters with respect to the trigger T. The counter voltages were set by first standardizing the light-pulser lamps in a standard counter, then using these standardized lamps to set the counter voltage so as to obtain the correct size output pulse.

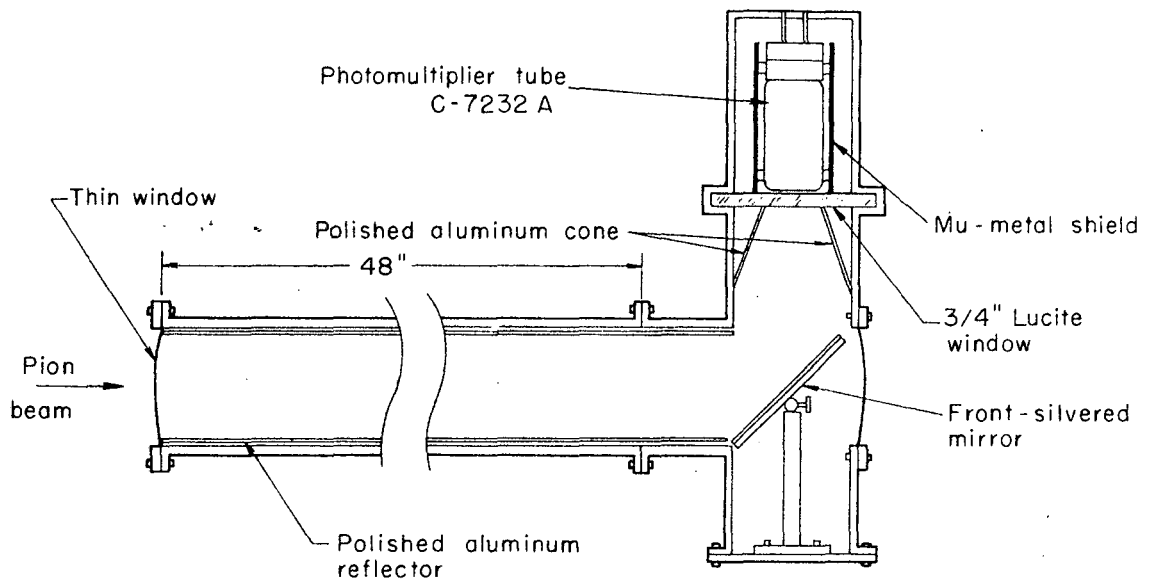
Some of the electronics leading to the matrix system was duplicated as a safety check to make sure it was working properly.

A master gate, controlled by the Bevatron magnetic cycle, caused the electronics to be operative only during the 200-msec interval that the pion beam was produced.

6. Cerenkov Counter

The gas Cerenkov counter shown in Fig. 14 was used to measure the muon and electron contamination in the pion beam. The counter was filled with sulfur hexafluoride (SF_6) gas, and is described in detail in reference 13.

During the measurement of the muon-electron contamination, and only then, the Cerenkov counter, C, was placed in the pion beam immediately downstream from the liquid-hydrogen target. A 2-in.-diam counter, M_4 , was placed in the beam at the downstream end of C. Its purpose was to insure that all particles detected by the counters traveled completely through C. The coincidences $M_1M_3M_4$ and $M_1M_3M_4C$ were counted. The ratio $M_1M_3M_4C/M_1M_3M_4$ gave a measure of the fraction of the beam that counted in C. Figure 15 is a plot of this ratio vs gas pressure (psig) in C. Three plateaus are shown in this figure. The plateau at the lower pressures is the result of only positive electrons counting. The next plateau is the result of both positive electrons and muons counting. The highest plateau is the result of all particles counting; i. e., positive electrons, muons, and pions. The curve in Fig. 15 gives a measure of the number of muons produced between the Bevatron target and the last bending magnet, B_2 . The number of muons produced downstream from B_2 had to be calculated. These muons were not momentum-analyzed and hence did not have a definite pressure threshold. Therefore they would only contribute a slope to the muon plateau. Curves similar to the one shown in Fig. 15 were determined for pion kinetic energies of 533, 698, 990, and 1555 MeV. The determination of the beam contamination is discussed in more detail in Sec. IIIB4.



MU-27659

Fig. 14. Gas Cerenkov Counter.

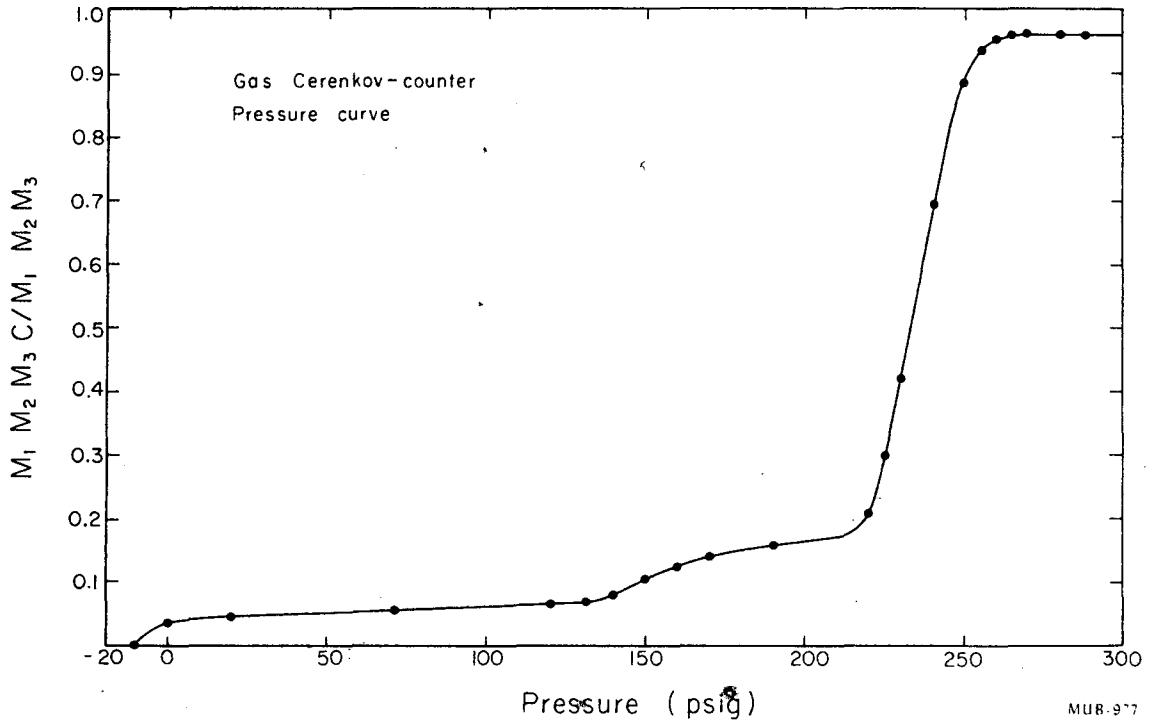


Fig. 15. Gas Cerenkov counter pressure curve taken at 698 MeV.

III. ANALYSIS OF DATA

A. General Analysis

The intensity, I , of the transmitted beam of pions after traversing the liquid hydrogen target is

$$I = I_0 \exp(-\sigma nx), \quad (1)$$

where

I_0 is the original intensity of the pion beam before entering the hydrogen target,

x is the average path length through the liquid hydrogen,

n is the number of protons per cm^3 ,

and

σ is the total cross section.

As was mentioned in Sec. IIB3, $nx = 4.196 \times 10^{23}$ protons/ cm^2 . The intensity of the transmitted pion beam can also be expressed as

$$I = I_0 - I_s - I_r, \quad (2)$$

where I_s is the intensity of the fraction of the beam that is elastically scattered, and I_r is the intensity of the fraction of the beam that undergoes a reaction. Solving Eq. (1) for σ , and using Eq. (2) to eliminate I , we obtain

$$\sigma = \frac{-1}{nx} \ln(1 - R - r), \quad (3a)$$

where $R = I_s/I_0$ and $r = I_r/I_0$. Since the liquid-hydrogen target was only 4 in. long, R and r are both small compared to 1. Therefore Eq. (3a) reduces to

$$\sigma = \frac{R}{nx} + \frac{r}{nx} \quad (3b)$$

Since the first term on the right side of Eq. (3b) includes all of the elastic scattering and nothing more, this term is obviously equal to the total elastic cross section.

In this experiment a contribution R_i was measured in each π_i counter. Each counter π_i was placed at an angle θ_i^* with respect

to the incident pion beam, and subtended a solid angle Ω_i^* . The asterisks refer to quantities in the c.m. system. This gave a measure of the differential cross section $d\sigma/d\Omega^*$, rather than total elastic cross section, where

$$\frac{d\sigma(\theta_i^*)}{d\Omega^*} = \frac{R_i}{n \times \Omega_i^*} \quad (4)$$

The denominator includes Ω^* to normalize the differential cross sections to unit solid angle in the c.m. system.

In this experiment there was scattering in the beam from material other than liquid hydrogen. This extraneous scattering had to be subtracted from the scattering by the full hydrogen target in order to obtain the scattering due to the liquid hydrogen alone. In terms of an equation,

$$R = \bar{R}_{\text{full}} - \bar{R}_{\text{empty}}, \quad (5)$$

where R represents the scattering from the liquid hydrogen alone, \bar{R}_{full} represents the scattering from the full hydrogen target, and \bar{R}_{empty} represents the scattering from the empty target. All these R 's are ratios of the counts in the π counter to the counts in the monitor system, or, in terms of coincidences,

$$R_i = \frac{M_1 M_2 M_3 S_0 \pi_i P_i}{M_1 M_2 M_3} \quad (6)$$

The subscript i stands for the i th elastic channel. Counter π_i is at an angle θ_i^* in the c.m. system. For convenience, the numerator in Eq. (6) will be replaced by the symbol π_i , and the denominator by M ; that is,

$$R_i = \frac{\pi_i}{M} \quad (7)$$

Many separate runs were made at each energy; some runs were made with

the target full, and the remainder with the target empty. The data from all full runs at each energy were added together to obtain

$$\bar{R}_{\text{full}} = \frac{\sum_{j=1}^n \pi_j}{\sum_{j=1}^n M_j} \quad (8)$$

where j represents the run number, and the summation is over full runs only. The channel number has been omitted for the sake of clarity. Similarly, \bar{R}_{empty} was calculated. The value of R for each individual run k was also calculated, by using the equation

$$R_k = \frac{\pi_k}{M_k} \quad (9)$$

Another ratio, similar to \bar{R} , was calculated:

$$\bar{R}_k = \frac{\sum_{j \neq k} \pi_j}{\sum_{j \neq k} M_j} \quad (10)$$

This is the average R with the k th run left out. The errors associated with \bar{R} , R_k , and \bar{R}_k are

$$\Delta \bar{R} = \frac{\left[\sum_{j=1}^n \pi_j \right]^{1/2}}{\sum_{j=1}^n M_j} \quad (11)$$

$$\Delta R_k = \frac{\left[\pi_k + 1 \right]^{1/2}}{M_k} \quad (12)$$

and

$$\Delta \bar{R}_k = \left[\frac{\sum_{j \neq k} M_j (R_j - \bar{R}_k)^2}{(n-2) \sum_{j \neq k} M_j} \right]^{1/2} \quad (13)$$

respectively. The errors $\Delta \bar{R}$ and ΔR_k are statistical, whereas $\Delta \bar{R}_k$ is a measure of the reproducibility of repeated runs. The error in \bar{R} associated with reproducibility was also calculated by using the equation

$$(\Delta \bar{R})_{\text{rep}} = \left[\frac{\sum_{j=1}^n M_j (R_j - \bar{R})^2}{(n-1) \sum_{j=1}^n M_j} \right]^{1/2} \quad (14)$$

This error was always nearly equal to or less than the statistical error $\Delta \bar{R}$, and hence was never used.

The residual of a run is defined as

$$\text{Res} = R_k - \bar{R} \quad (15)$$

This is the deviation of the kth run from the average. Another type of residual was calculated by using the equation

$$\text{Res}_k = R_k - \bar{R}_k \quad (16)$$

This is the deviation of the kth run from the average of the rest of the runs. The data for a particular run and a particular elastic channel were rejected if

$$\left| \text{Res}_k \right| > 3 (\Delta R_k + \Delta \bar{R}_k) \quad (17)$$

Less than 0.1% of the data was rejected because of this criterion.

The statistical error associated with the differential cross section $d\sigma/d\Omega^*$ is

$$\Delta_s = \frac{1}{n \times \Omega^*} \left[(\Delta \bar{R}_{\text{full}})^2 + (\Delta \bar{R}_{\text{empty}})^2 \right]^{1/2}, \quad (18)$$

where $\Delta \bar{R}$ is as defined in Eq. (11).

Combining Eqs. (4) and (5), we obtain the basic equation for the differential cross section:

$$\frac{d\sigma(\theta^*)}{d\Omega^*} = \frac{1}{n \times \Omega^*} (\bar{R}_{\text{full}} - \bar{R}_{\text{empty}}), \quad (19)$$

where \bar{R} is as defined in Eq. (8). Various corrections were applied to Eq. (19) to get the final data. The statistical error from Eq. (18) was combined with the other errors resulting from the applied corrections to get the final errors in the data points. These corrections and their errors are discussed in the next section.

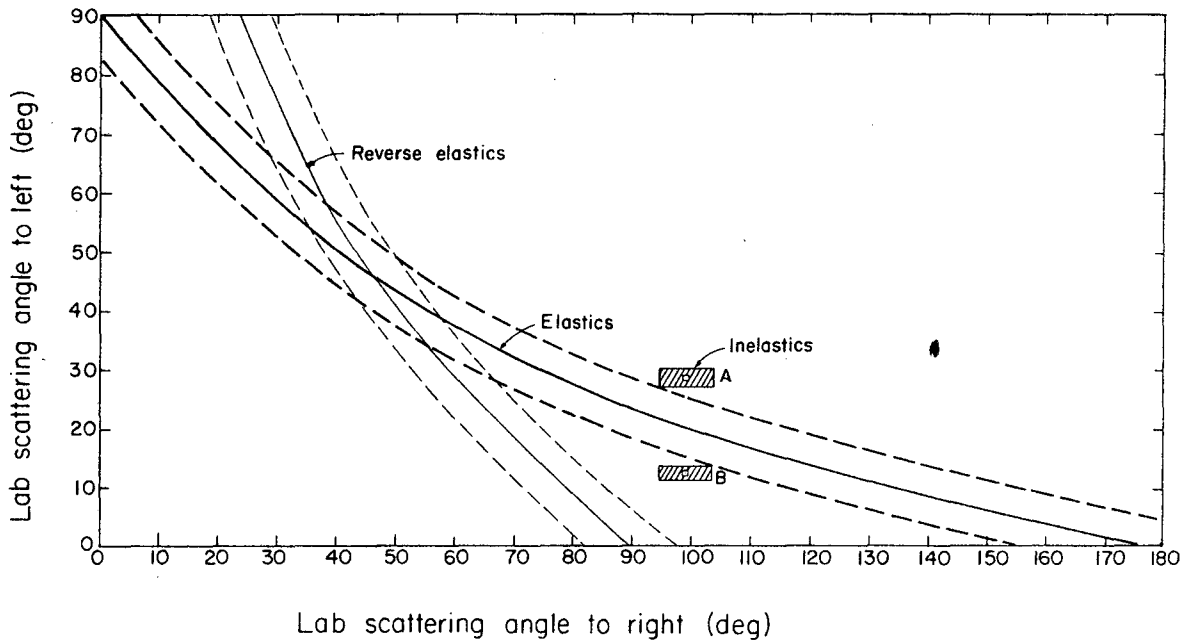
B. Corrections to Data

1. Inelastic Scattering

An inelastic pion-proton scattering event is defined as a scattering event for which the final state consists of something other than a single pion and a single proton. The counter system used in this experiment was designed to minimize inelastics and still get sufficient elastic data. However it was not possible to eliminate inelastics altogether, so they did occasionally contribute to the elastic kinematic channels.

A measure of the charged inelastic events was made during the experiment by recording coincidences between π and p counter pairs for which no elastic events could contribute counts.

Figure 16 shows the kinematical relationship between the pion lab angle and the proton lab angle, both for the pion going to the right (heavy solid line), and for the pion going to the left (light solid line). In this experiment elastic events were measured with the pion going to



MU 27661

Fig. 16. Pion-proton elastic kinematic curves showing band where elastic data were collected, two of the 42 regions where inelastic data were collected, and region where reverse-elastic band overlaps elastic band.

the right. Because of the finite size of both the π and P counters, these kinematic curves are spread out into bands, as indicated by the dashed curves in Fig. 16. Areas A and B in Fig. 16 are examples of π - p counter pairs that are outside the elastic bands. Inelastic events were measured in 42 areas, such as A and B, all of which were in fairly close proximity to the heavy dashed elastic band. The data from these 42 inelastic channels were normalized by dividing R_d , the ratio of counts in the inelastic channel to monitor counts, by the lab solid angles of both the π and the p counter. The resulting quotient Z_d is the number of inelastic counts per unit monitor count per unit solid angle, both left and right. Let the Z axis be normal to the plane defined in Fig. 16. A surface $Z(x,y)$ was least-squares-fitted¹⁴ to the data points Z_d by using an equation of the form

$$Z(x, y) = A_0 + A_1(x+y) + A_2xy + A_3(x^2 + y^2) + A_4(x^2y + xy^2) + \dots,$$

where $x = \cos \theta_{\text{right}}$ and $y = \cos \theta_{\text{left}}$. A sufficient number of terms was used to obtain a reasonable fit. Usually, it was only necessary to use those terms up to and including $A_3(x^2 + y^2)$. An equation that is symmetric in x and y was used, because the inelastic scattering is symmetric with respect to scattering left and right. Powers of $\cos \theta$ were used, rather than powers of θ , in order to make the surface for the region $0 \text{ deg} < \theta < 180 \text{ deg}$ agree with the surface for the region $360 \text{ deg} > \theta > 180 \text{ deg}$.

The value, Z_k , of Z at the coordinates corresponding to the k th elastic-channel point (lying on the heavy solid curve) was determined, and then multiplied by the lab solid angles of both the π_k and the P_k counters. The resultant product IC_k is the inelastic correction for the k th elastic channel. Equation (19) then becomes

$$\frac{d\sigma(\theta^*)}{d\Omega^*} = \frac{1}{n_x \Omega^*} (\bar{R}_{\text{full}} - \bar{R}_{\text{empty}} - IC) \quad (20)$$

for each elastic channel.

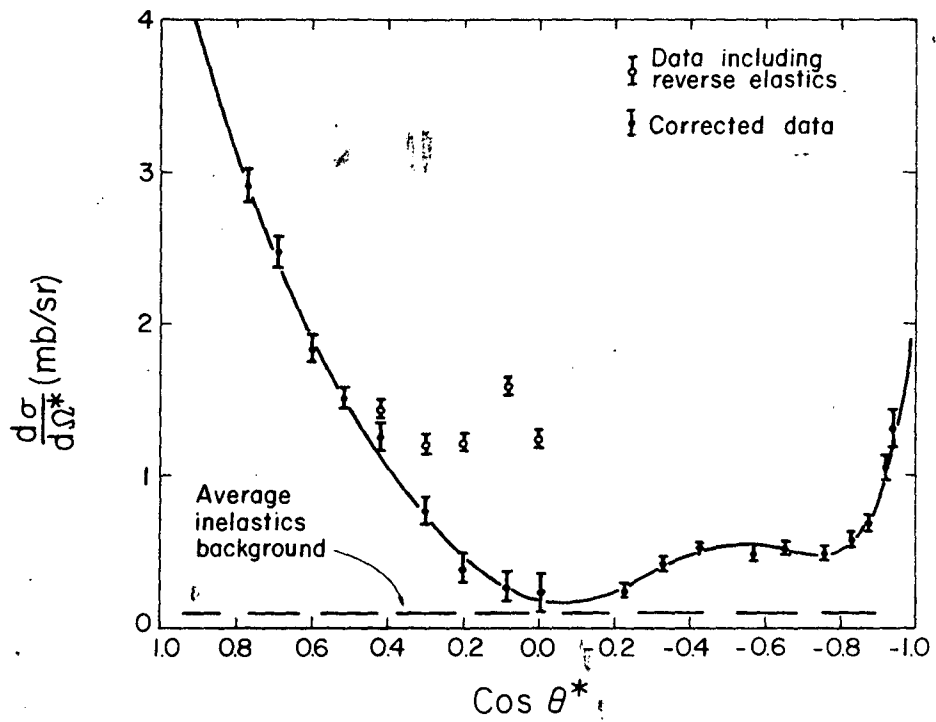
The statistical error in R_d , as calculated by using Eq. (11) of the previous section, was normalized to unit solid angle, both left and right. The resultant errors in Z_d were used to make the least-squares fit. The error matrix determined in the least-squares method was then used to get the errors in Z_k . These errors were multiplied by the appropriate solid angles to obtain the errors ΔIC_k in the various IC_k . The errors ΔIC_k were then combined with $\Delta \bar{R}_{full}$ and $\Delta \bar{R}_{empty}$ in Eq. (18) by taking the sum of the squares of the errors (Eq. 21). The error in the differential cross section for each elastic channel then becomes

$$\Delta \sigma = \frac{1}{n \times \Omega^*} \left[(\Delta \bar{R}_{full})^2 + (\Delta \bar{R}_{empty})^2 + (\Delta IC)^2 \right]^{1/2} \quad (21)$$

Figure 17 shows the relative magnitudes of the elastic data (solid curve) and the average charged inelastic background (dashed curve) as measured at a pion lab kinetic energy of 990 MeV.

2. Accidentals

A coincidence circuit being fed by two counters will put out an accidental count whenever the two coincidence inputs each simultaneously receive a random pulse, where these two random pulses are unrelated in every respect except for being coincident in time. Accidentals in coincidences which are more than two-fold are also possible, but these occur much less frequently. Usually the most predominant type of accidental in a three-fold coincidence is one where two of the pulses are definitely related, and the third is random. This type of accidental could have resulted in a considerable ($\approx 4\%$) correction to the monitor counts in this experiment, except for the fact that the monitor system was "protected" against this type of accidental by the double-pulse-rejection system. Because M_1 and M_2 were large compared to the size of the beam, the worst type of accidental would have been caused by one beam particle giving M_1 and M_2 related pulses, but missing M_3 and a second beam particle giving M_3 a random time-correlated pulse.



MU-27617

Fig. 17. Differential-cross-section curve for an incident pion lab kinetic energy of 990 MeV, including corrected data points with errors, data points before reverse-elastics correction was applied, and average inelastic background.

This type of accidental could not have been counted, however, because both particles, being closely spaced in the beam, would have caused the double-pulse-rejection system to reject this accidental count.

Other types of accidentals in the monitor system were estimated to be negligible.

Accidentals in the elastic and inelastic channels were measured in several cases, including those channels fed by the π and ρ counters with the highest singles counting rate, and in all cases it was found that these accidentals were also negligible.

3. Reverse Elastics

As was previously mentioned, the heavy dashed lines in Fig. 1b indicate the region where elastic data were taken at a particular energy. The region bounded by the light dashed lines is called the reverse-elastics region, because the pion scatters toward the proton counters and the proton recoils toward the pion counters. In the relatively small area where the reverse-elastic band overlaps the elastic band, reverse-elastic counts are recorded in those elastic channels. In this overlap area, the pion counts in a proton counter say P_k , and the recoil proton counts in the corresponding π_k counter.

Pulses, from π and ρ counters, that resulted from reverse-elastic events had the proper time relationship, just as the pulses from true elastic events did. This was because of the relatively wide (35- μ sec) gate to the coincidence matrix system and the "slow" coincidence circuits in the matrix system.

In order to determine the fraction of reverse-elastic counts recorded in the k th elastic channel, it is necessary to determine the following quantities in the c. m. system:

- (a) the effective solid angle Ω_R for accepting a pion in counter P_k when the recoil proton also enters counter π_k ; i. e., the effective solid angle for a reverse-elastic event
- (b) the effective solid angle Ω_F of counter π_k
- (c) the average scattering angle θ_R of the reverse-scattered pions that are counted in counter P_k

- (d) the angle of scattering θ_F to the center of counter π_k
- (e) the values of the differential cross section at the reverse scattering angle θ_R and the forward scattering angle θ_F .

The quantities Ω_F and θ_F were determined by the placement and size of counter π_k .

The quantities Ω_R and θ_R were determined with the aid of an IBM 7090 computer, by using the following information:

- (a) the sizes and positions of counters π_k and P_k
- (b) the size and position of the hydrogen target
- (c) the kinematics of the scattering
- (d) the momentum distribution across the 6% momentum spread
- (e) the amount of convergence of the pion beam
- (f) the beam profile
- (g) the shape of the LH_2 target vessel. This information was fairly well known, hence the quantities Ω_R and θ_R were determined with reasonable accuracy.

After the reverse-elastic correction is applied, we obtain the values of the differential cross sections at the angles θ_F and θ_R as final results. A difficult situation is created, because we need to know the final result in order to obtain the correction, which precedes the final results. The problem is made less difficult by the fact that only a few of the elastic channels need this type of correction. Because of the "bootstrap" nature of this correction, it was the final correction that was applied to the data.

After all of the other corrections have been applied, the total counting rate R_0 in a particular elastic channel is equal to the sum of the contribution from forward elastic events R_F and the contribution from reverse-elastic events R_R . By using Eq. (4) of Sec. IIIA we obtain

$$\Omega_F \sigma_\sigma(\theta_F) = \Omega_F \sigma(\theta_F) + \Omega_R \sigma(\theta_R), \quad (22)$$

where $\sigma(\theta)$ is the differential cross section corrected for reverse elastics, i. e., $d\sigma(\theta)/d\Omega$, and $\sigma_0(\theta)$ is the uncorrected differential cross section.

Rearranging terms, we obtain

$$\sigma(\theta_F) = \sigma_0(\theta_F) - H\sigma(\theta_R), \quad (23)$$

where

$$H = \Omega_R / \Omega_F. \quad (24)$$

the last term in Eq. (23), i. e., H multiplied by the corrected cross section at the reverse angle, is the reverse-elastic correction. This correction must be subtracted from the uncorrected cross section σ_0 in order to obtain the corrected cross section $\sigma(\theta_F)$ at the forward angle.

It would be desirable to use Eq. (23) in an iterative procedure; however, in its present form, the iteration would diverge whenever H is greater than one, which frequently occurs. By a suitable manipulation it is possible to rearrange Eq. (23) into the following form:

$$\sigma(\theta_F) = G\sigma_0(\theta_F) + GH[\sigma(\theta_F) - \sigma(\theta_R)], \quad (25)$$

where $G = 1/(1+H)$. The $\sigma(\theta)$ on the left side of Eq. (25) can be considered as the "new" approximation, which is calculated by putting the "old" approximation in the right-hand side. An iteration procedure using Eq. (25) will converge for any positive value of H , because in this case it is equivalent to a power series in (GH) , where (GH) is less than one whenever H is positive. The rate of convergence is enhanced by the fact that the last term in Eq. (25) is very small, because $\sigma(\theta_R) \approx \sigma(\theta_F)$. Equation (25) was used to correct the cross sections for reverse-elastic events, although Eq. (23) was also satisfied at the end of the iteration process.

The final error on $\sigma(\theta_F)$, as given in Eq. (23), is

$$\Delta\sigma(\theta_F) = \left\{ [\Delta\sigma_0(\theta_F)]^2 + H^2 [\Delta\sigma(\theta_R)]^2 + [\sigma(\theta_R)]^2 (\Delta H)^2 \right\}^{1/2}, \quad (26)$$

where $\Delta\sigma_0(\theta_F)$ contains all of the other errors, (ΔH) is the error on H , and $\Delta\sigma(\theta_R)$ is the error on the fitted curve at the angle θ_R . With

H^2 being larger than two in some cases, the middle term on the right-hand side of Eq. (26) can be a sizeable contribution to the error.

Figure 17 shows the data at 990 MeV both before and after correction for reverse elastics.

4. Beam Contamination

Positive muons were produced in the pion beam by the decay of pions. Those muons produced between the Bevatron target and B_2 were momentum-analyzed by the effects of B_1 , B_2 , and the quadrupoles, and were measured with a gas Cerenkov counter as described in Sec. IIB6. The number of muons produced between B_2 and the LH_2 target was calculated by dividing this part of the beam into small segments, calculating the number of pions decaying in each segment, determining the number of the resultant muons that went through counter M_3 , and summing the contributions from each segment. Consider a segment extending from X_1 to X_2 , where X is the distance from the Bevatron target along the beam. The number of muons produced in such a segment is

$$n = n_0 \left[\exp\left(\frac{-X_1}{X_L}\right) - \exp\left(\frac{-X_2}{X_L}\right) \right], \quad (27)$$

where X_L is the distance the pions travel during their mean life; however, not all of these muons pass through M_3 .

Neutral pions produced in the Bevatron target predominantly decayed into photons before they emerged from the target. These photons often produced electron pairs in the Bevatron target. The resulting positive electrons having the correct momentum and heading in the correct direction contributed to the electron contamination in the beam. This was the major source of electron contamination. The electron contamination was also measured with the gas Cerenkov counter.

The proton contamination was less than 0.1% at the highest energy, and much less than that at lower energies. (This is discussed in Sec. IIB5.)

Contamination from K^+ mesons was negligible because the K mesons decayed before they reached the LH_2 target.

The beam at the LH_2 target thus essentially consisted of pions, muons, and electrons. Figure 18 shows the fraction of the total beam comprised of electrons, muons produced before B_2 , and muons produced after B_2 . The total muon and electron contamination varied from 5.6% of the total beam at the highest energy, to 15.3% at the lowest energy.

Since the cross sections for muons and electrons interacting in the LH_2 target are so small, the only appreciable effect they had was to cause the monitor system to count too high. This was corrected for by reducing the number of monitor counts so as to include only pions.

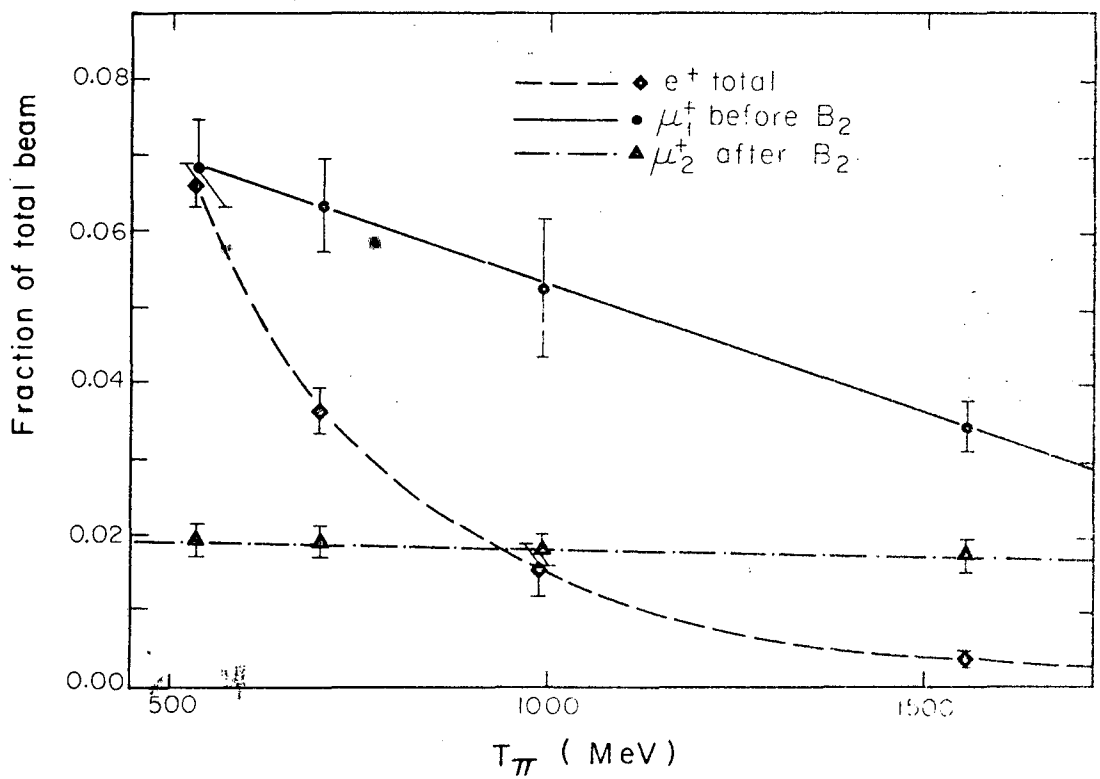
5. Miscellaneous Corrections and Errors

Several small corrections were applied to the data in addition to those already mentioned.

The S_0 counter was "dead" 0.5% of the time; however, the monitor system had no corresponding dead time. Therefore, the number of monitor counts had to be reduced 0.5% to compensate for this effect.

The number of monitor counts was also reduced by about 1%, because approximately 1% of the pions were scattered out of the beam by the liquid hydrogen before they reached the center of the LH_2 target, i. e., the effective center of scattering. This correction factor depended upon the energy of the incident pion beam.

The values of the measured differential cross section data points were increased about 1%, because either the scattered pion or the recoil proton could rescatter before they reached their appropriate counters. The magnitude of this correction factor depends on the energies of the scattered pion and recoil proton, the scattering cross sections, the solid angles of the π and P counters, and the amount of material on which the pion and proton might scatter.



MU 27652

Fig. 18. Muon and electron contamination in pion beam plotted vs incident pion lab kinetic energy.

Another correction to the data points was applied to compensate for the fact that the data for a given angle were actually collected over a finite angular range, where the given angle is the center of the angular range. The magnitude of this multiplicative correction factor is

$$A = \frac{\sigma(\theta_c)}{\langle \sigma(\theta) \rangle_{av}}, \quad (28)$$

where $\sigma(\theta_c)$ is the value of the differential cross section at the central angle, and $\langle \sigma(\theta) \rangle_{av}$ is the average value of the differential cross section across the finite angular range. Both $\sigma(\theta_c)$ and $\langle \sigma(\theta) \rangle_{av}$ were determined from a fitted curve that was essentially identical to the final fitted curve. If $A = 1$ there is no correction; if $A = 0$ or $A = 2$ a 100% correction is applied. The term A can easily be quite different from 1 when the magnitude of $\sigma(\theta_c)$ is very small.

In this experiment, A was usually about 1. However, in some cases A was quite different from 1. In one particular case A was equal to 0.42; in this case the value of $\sigma(\theta_c)$ was nearly zero. The actual magnitude of the change of $d\sigma/d\Omega^*$, when this correction was applied, was always small.

The largest contributions to the errors quoted on the data points came from the statistical errors [Eq. (18) in Sec. IIIA] and from the reverse-elastics error. Equation (26) in Sec. IIIB3 shows a typical example of how the errors on the various terms in Eq. (23) are combined. Contributions to the errors resulted from each of the various corrections to the data, and from the uncertainty in the angles to the centers of the π counters and the uncertainties in the solid angles of the π counters.

At 990 MeV the data point at $\cos \theta^* \approx +0.3$ (Fig. 17) might be considered a typical point that includes reverse elastics. With 91.3×10^6 pions incident on the full LH_2 target, 1363 events were recorded in this channel. With 50.4×10^6 pions incident on the empty target vessel, 142 events were recorded in this channel, indicating that approximately 19% of the 1363 "target full" events came from the

target vessel. The remaining 1105 events were LH_2 scattering events. Approximately 7% of these 1105 events were inelastic events, and approximately 32% were reverse-elastic events, leaving 672 true elastic events for this channel. Approximately 16 000 true elastic events were recorded for the 19 channels at 990 MeV.

The final data, including errors, are quoted in the next section.

IV. EXPERIMENTAL RESULTS

A. Differential-Cross-Section Data

The elastic differential cross sections are listed in Tables IV through X, together with the errors (standard deviations), and the cosines of the scattering angles in the c.m. system. The values listed for $\cos\theta^* = 1.0$ were calculated by using dispersion relations.¹⁵

Although data were taken at 21 different angles at each energy, the data at some of these angles were rejected. At small angles of scattering, the recoil protons did not have enough energy to reach the proton counters. This eliminated the first 5 angles at 533 MeV, 4 at 581 MeV, 3 at 698 MeV, 2 at 873 MeV, and 1 at both 990 and 1311 MeV. The data from channel 11 seemed to have a systematic error of unknown origin in them. As a result, the differential cross sections for this channel were significantly too large at all energies. The probability of such a phenomenon occurring naturally is extremely small, and hence the data from channel 11 were also rejected.

B. Cosine Fits

A curve having the equation

$$\frac{d\sigma(\theta^*)}{d\Omega^*} = \sum_{n=0}^N a_n \cos^n \theta^* \quad (29)$$

was least-squares-fitted to the data points.¹⁴ The fitted curves, along with the data points, are shown in Figs. 19 through 25. The dispersion-relations point was used to make the final fit at all energies. A fourth-order fit, i. e., $N = 4$, was used at the lower three energies of this experiment; a seventh-order fit was used at the higher four energies.

Table IV. Differential-cross-section data and errors
in standard deviations for $T_{\pi} = 533$ MeV.

$\text{Cos } \theta^*$	$\frac{d\sigma(\theta^*)}{d\Omega^*}$
1.000	4.800±0.648
0.547	2.389±0.064
0.446	1.906±0.074
0.363	1.482±0.074
0.259	1.202±0.075
0.155	0.793±0.122
-0.062	0.348±0.031
-0.173	0.156±0.023
-0.276	0.071±0.020
-0.445	0.054±0.019
-0.551	0.060±0.018
-0.675	0.090±0.021
-0.768	0.142±0.022
-0.836	0.217±0.029
-0.885	0.157±0.035
-0.925	0.145±0.035

Table V. Differential-cross-section data and errors
in standard deviations for $T_{\pi} = 581$ MeV.

$\text{Cos } \theta^*$	$\frac{d\sigma(\theta^*)}{d\Omega^*}$
1.000	3.470±0.742
0.613	2.163±0.056
0.533	2.032±0.054
0.429	1.512±0.071
0.345	1.019±0.082
0.239	0.807±0.091
0.135	0.589±0.131
-0.083	0.259±0.022
-0.193	0.086±0.019
-0.295	0.020±0.019
-0.461	0.046±0.018
-0.565	0.090±0.017
-0.686	0.127±0.018
-0.776	0.156±0.019
-0.842	0.113±0.022
-0.890	0.153±0.023
-0.928	0.079±0.028

Table VI. Differential-cross-section data and errors
in standard deviations for $T_{\pi} = 698$ MeV.

$\text{Cos } \theta^*$	$\frac{d\sigma(\theta^*)}{d\Omega^*}$
1.000	2.250±0.542
0.664	1.426±0.050
0.583	1.221±0.044
0.499	1.041±0.046
0.391	0.694±0.048
0.303	0.607±0.049
0.195	0.375±0.050
0.089	0.156±0.072
-0.129	0.130±0.026
-0.237	0.113±0.021
-0.336	0.115±0.023
-0.497	0.208±0.025
-0.596	0.264±0.022
-0.710	0.267±0.023
-0.794	0.272±0.027
-0.855	0.195±0.032
-0.899	0.239±0.035
-0.934	0.186±0.045

Table VII. Differential-cross-section data and errors
in standard deviations for $T_{\pi} = 873$ MeV.

$\text{Cos } \theta^*$	$\frac{d\sigma(\theta^*)}{d\Omega^*}$
1.000	3.800±0.453
0.709	2.339±0.081
0.627	1.788±0.072
0.540	1.549±0.065
0.450	1.279±0.066
0.336	0.854±0.103
0.246	0.551±0.103
0.134	0.278±0.090
0.027	0.254±0.116
-0.190	0.141±0.039
-0.295	0.095±0.041
-0.391	0.172±0.042
-0.542	0.265±0.046
-0.635	0.397±0.047
-0.740	0.385±0.045
-0.816	0.447±0.053
-0.871	0.413±0.063
-0.910	0.575±0.069
-0.942	0.854±0.100

Table VIII. Differential-cross-section data and errors
in standard deviations for $T_{\pi} = 990$ MeV.

$\text{Cos } \theta^*$	$\frac{d\sigma(\theta^*)}{d\Omega^*}$
1.000	4.780±0.410
0.770	2.934±0.090
0.690	2.470±0.079
0.604	1.838±0.070
0.513	1.518±0.061
0.420	1.265±0.078
0.303	0.777±0.092
0.210	0.407±0.086
0.097	0.268±0.085
-0.011	0.238±0.146
-0.226	0.247±0.046
-0.329	0.423±0.043
-0.422	0.502±0.046
-0.568	0.485±0.052
-0.657	0.532±0.041
-0.756	0.495±0.047
-0.828	0.596±0.049
-0.880	0.688±0.065
-0.917	1.068±0.078
-0.946	1.308±0.124

Table IX. Differential-cross-section data and errors
in standard deviations for $T_{\pi} = 1311$ MeV.

$\text{Cos } \theta^*$	$\frac{d\sigma(\theta^*)}{d\Omega^*}$
1.000	14.030±0.818
0.731	1.796±0.081
0.640	0.879±0.063
0.543	0.512±0.053
0.443	0.254±0.056
0.342	0.466±0.091
0.218	0.405±0.097
0.121	0.190±0.090
0.006	0.362±0.076
-0.101	0.386±0.075
-0.310	1.182±0.065
-0.407	1.355±0.068
-0.494	1.288±0.076
-0.627	1.091±0.076
-0.705	0.917±0.065
-0.793	0.702±0.071
-0.855	0.757±0.085
-0.899	1.162±0.102
-0.930	1.504±0.131
-0.955	1.927±0.180

Table X. Differential-cross-section data and errors
in standard deviations for $T_{\pi} = 1555$ MeV.

$\text{Cos } \theta^*$	$\frac{d\sigma(\theta^*)}{d\Omega^*}$
1.000	11.180±0.776
0.832	3.537±0.120
0.702	1.155±0.071
0.603	0.458±0.056
0.500	0.302±0.062
0.394	0.395±0.073
0.289	0.464±0.075
0.161	0.382±0.076
0.063	0.337±0.074
-0.053	0.257±0.071
-0.160	0.260±0.070
-0.363	0.496±0.061
-0.456	0.582±0.065
-0.537	0.419±0.067
-0.662	0.266±0.073
-0.734	0.178±0.079
-0.814	0.005±0.033
-0.870	0.085±0.076
-0.910	0.098±0.124
-0.938	0.152±0.177
-0.960	0.679±0.195

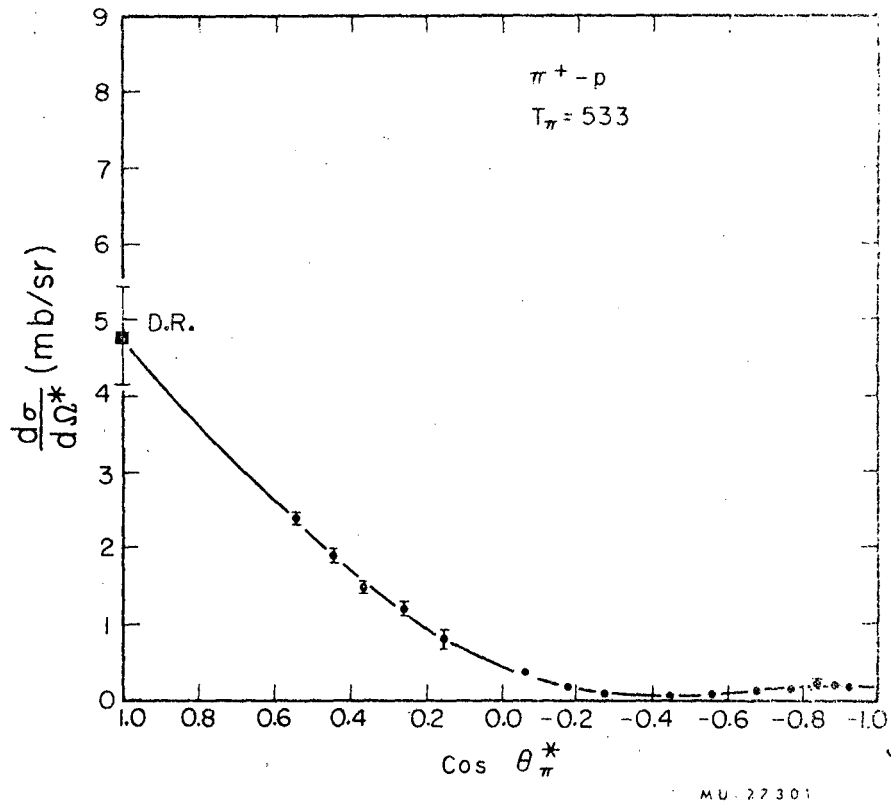


Fig. 19. The $\pi^+ - p$ differential-cross-section curve for an incident pion lab kinetic energy of 533 MeV.

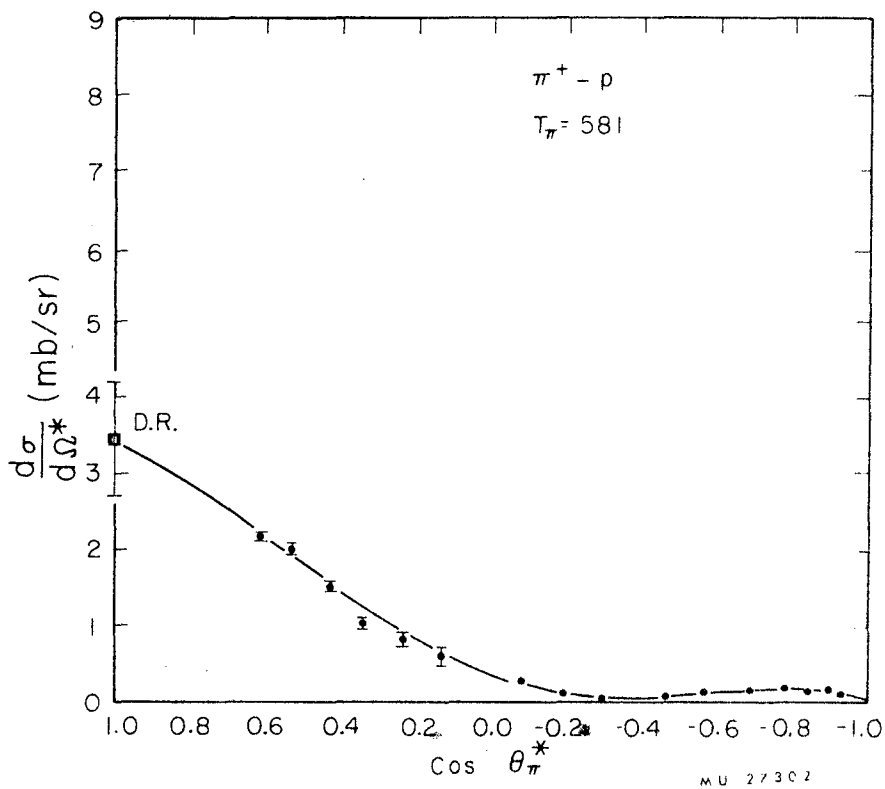


Fig. 20. The π^+ -p differential-cross-section curve for an incident pion lab kinetic energy of 581 MeV.

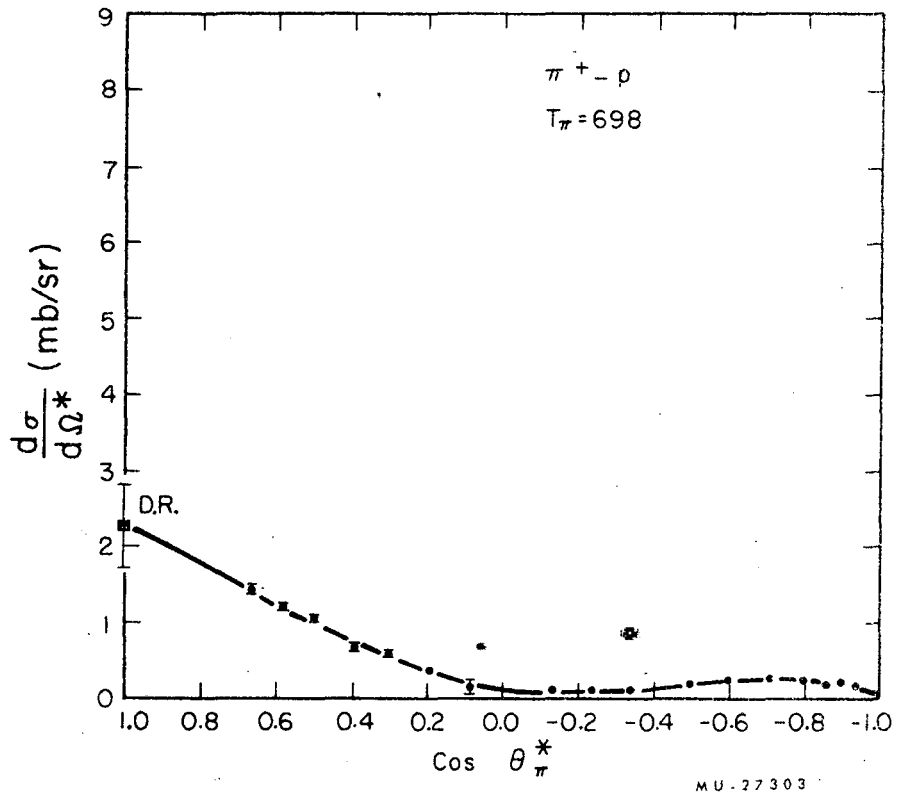
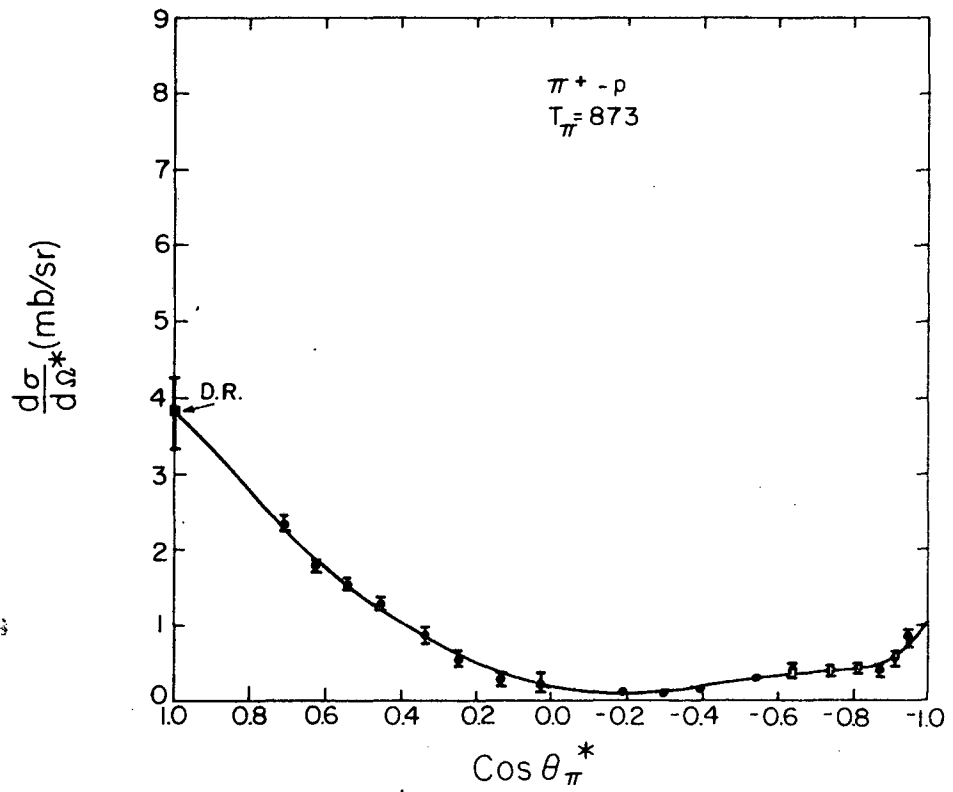


Fig. 21. The π^+ -p differential-cross-section curve for an incident pion lab kinetic energy of 698 MeV.



MU-27310

Fig. 22. The π^+ -p differential-cross-section curve for an incident pion lab kinetic energy of 873 MeV.

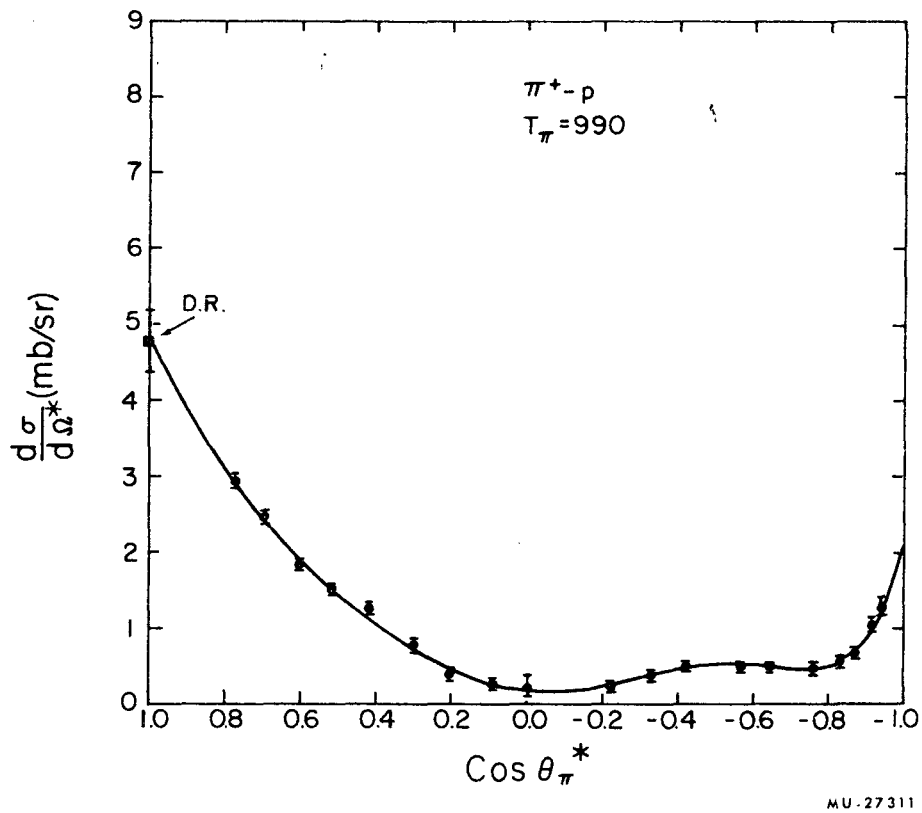
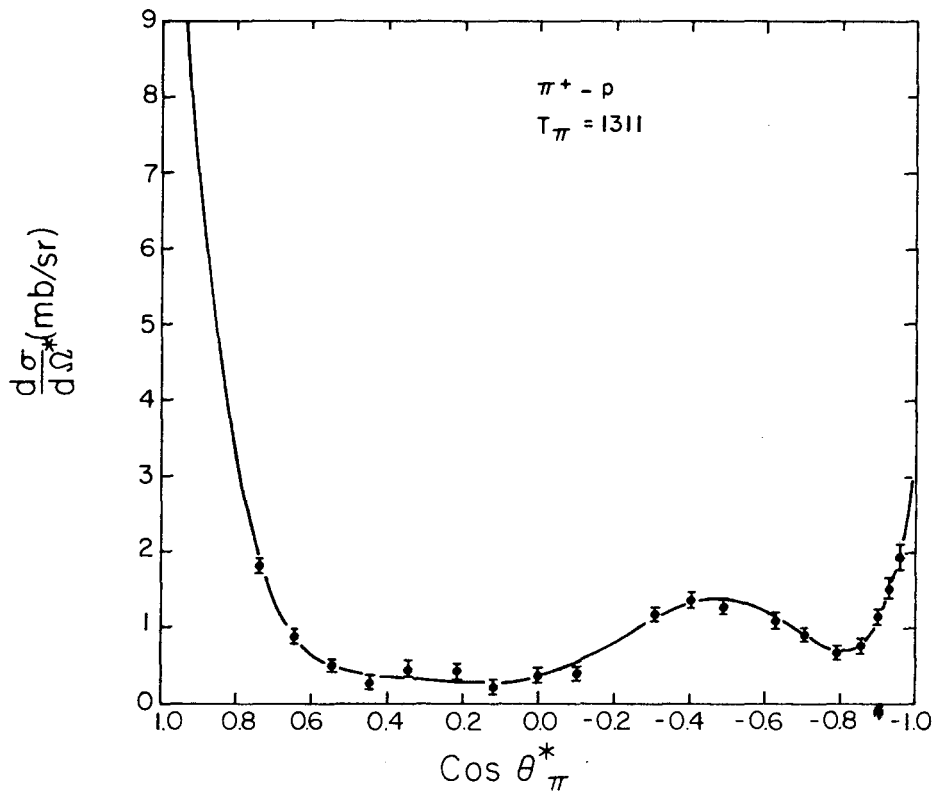


Fig. 23: The $\pi^+ - p$ differential-cross-section curve for an incident pion lab kinetic energy of 990 MeV.



MU-27312

Fig. 24. The π^+ -p differential-cross-section curve for an incident pion lab kinetic energy of 1311 MeV.

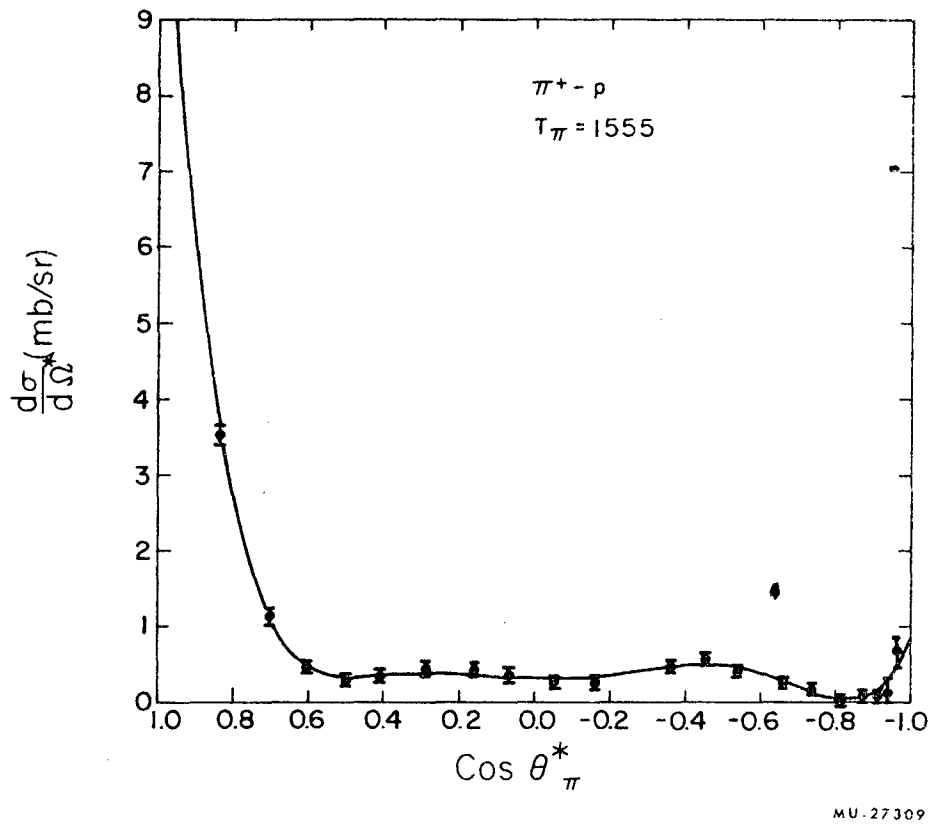


Fig. 25. The π^+ -p differential-cross-section curve for an incident pion lab kinetic energy of 1555 MeV.

The determination of the correct order of fit to be used is a rather difficult problem. One criterion that was used is that if a k th order fit is needed at some particular energy, then at higher energies the order of fit should never be less than k . The basis for this criterion is that if a specific ℓ th partial wave is needed at a certain energy, this ℓ th partial wave should also be present at all higher energies even though its contribution may be very small. As used here, ℓ is the orbital-angular-momentum quantum number.

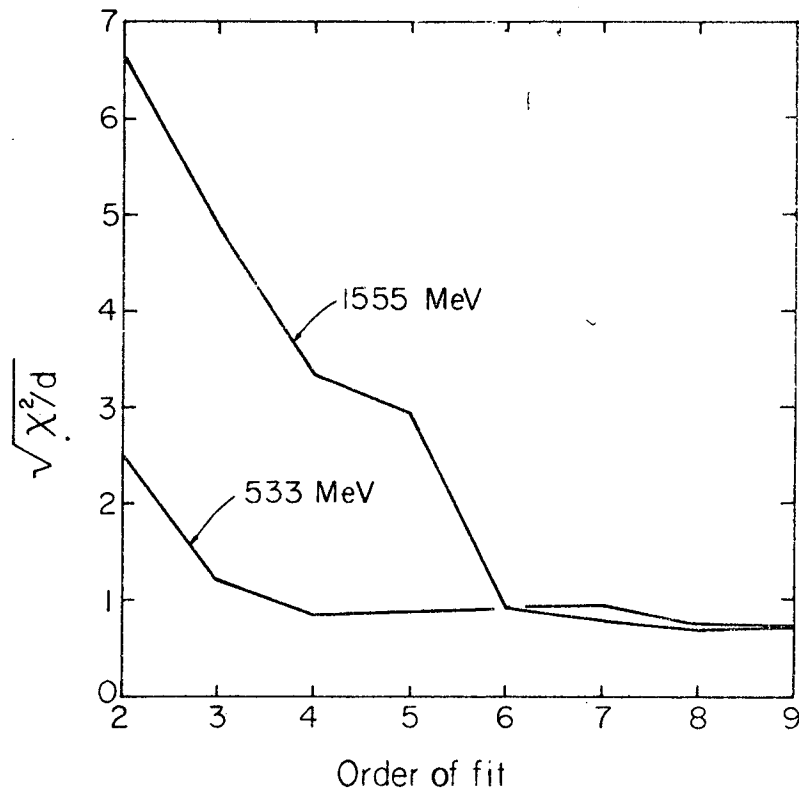
Another criterion used was to choose that order of fit which gave the best agreement between the curves fitted with and without the dispersion-relations point.¹⁵ This was probably the most important criterion.

At 873 MeV the data could statistically be fitted with a third-order fit. However, a third-order fit did not produce the sharp rise at $\cos \theta^* = -1$, as indicated by the data points. A seventh-order fit was the lowest-order fit, made without the dispersion relations point that both produced the sharp rise at $\cos \theta^* = -1$, and also had the correct value at $\cos \theta^* = +1$. This sharp rise at $\cos \theta^* = -1$ becomes more pronounced at 990 MeV, very pronounced at 1311 MeV, and starts to diminish again at 1555 MeV.

Naturally, the standard statistical tests, such as the χ^2 test and the Fisher "F" test,¹⁴ were taken into consideration, but they were sometimes misleading. Figure 26 shows the values of $(\chi^2/d)^{1/2}$, the "goodness-of-fit" parameter, plotted vs the order of fit N . These plots are for the lowest energy, 533 MeV, and the highest energy, 1555 MeV, where d is the number of degrees of freedom; i. e.,

$$d = P - (N + 1), \quad (30)$$

where P is the number of data points to which the curve is fitted.



MU-27618

Fig. 26. Curves showing goodness-of-fit parameter $(\chi^2/d)^{1/2}$ plotted vs order of fit for the lowest and highest energies of the experiment.

Figure 26 seems to indicate that a sixth-order fit is sufficient at 1555 MeV; however, a seventh-order fit was chosen because that is the order of fit needed at a lower energy, 873 MeV.

Table XI gives the values of χ^2 and $(\chi^2/d)^{1/2}$ for the chosen fit at each energy.

The values of the coefficients a_n and their errors are listed in Table XII, and are shown plotted in Fig. 27 with pion laboratory kinetic energy as the abscissa.

C. Total Elastic Cross Sections

The total elastic cross sections, obtained from the differential elastic cross section data by integrating under the fitted curves, are listed in Table XI, along with their errors. Figure 28 shows the total elastic cross section plotted vs pion lab kinetic energy. Also shown in this figure are the total cross section³ and the total inelastic cross section; i. e., the difference between the total cross section and the total elastic cross section.

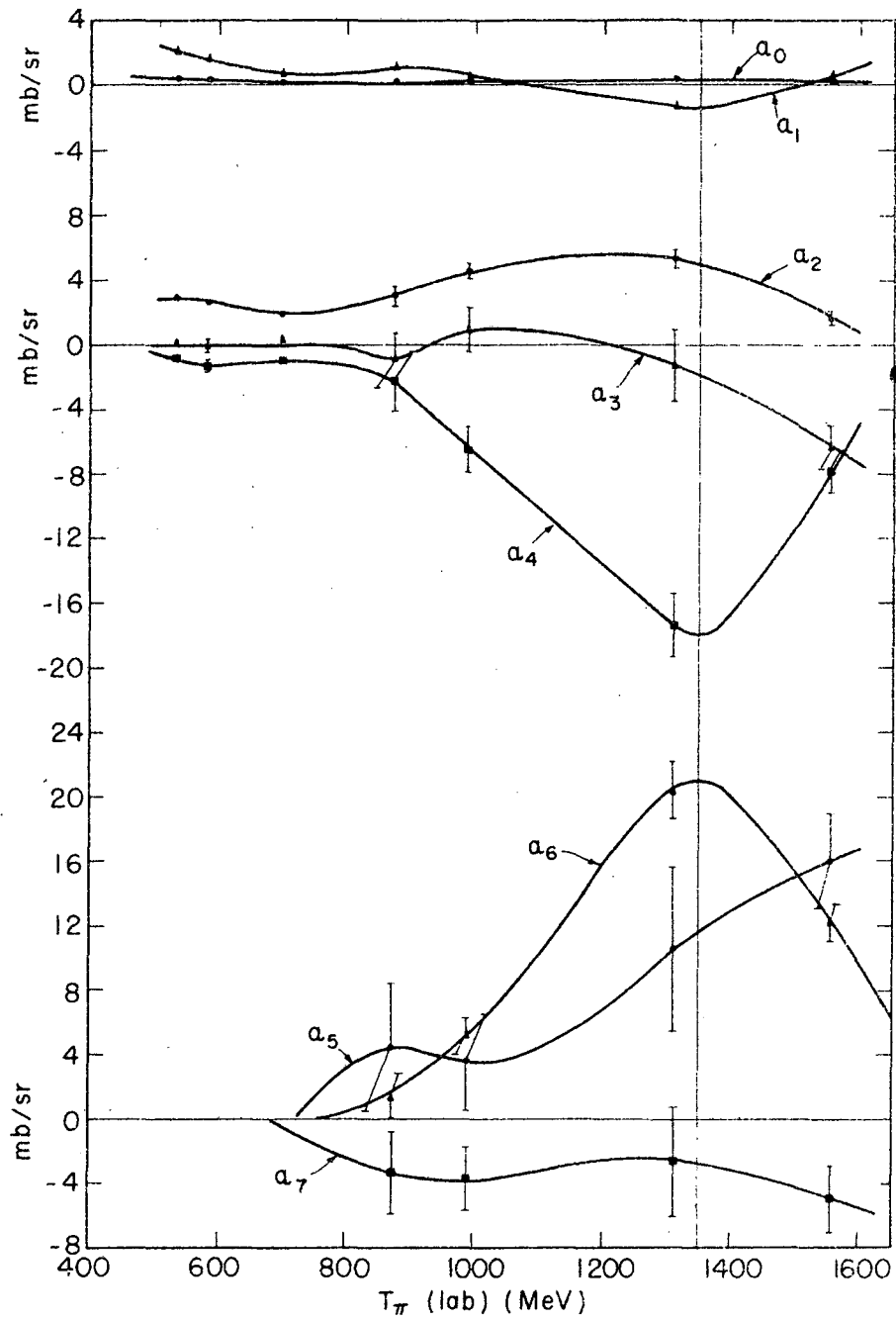
Table XI. Values of χ^2 , $(\chi^2/d)^{1/2}$, the number of data points,^a the number of degrees of freedom, and the total elastic cross section with its error at each energy of the experiment.

Energy (MeV)	χ^2	$(\chi^2/d)^{1/2}$	Number of data points	Degrees of freedom	Elastic cross section
533	7.89	0.85	16	11	15.32±0.47
581	25.26	1.45	17	12	12.17±0.57
698	9.28	0.84	18	13	8.02±0.22
873	13.96	1.13	19	11	12.05±0.45
990	11.33	0.97	20	12	14.54±0.31
1311	16.92	1.19	20	12	19.31±0.61
1555	8.36	0.80	21	13	13.04±0.28

^aThe dispersion-relations point, having been used in the curve fitting, is included in the number of data points.

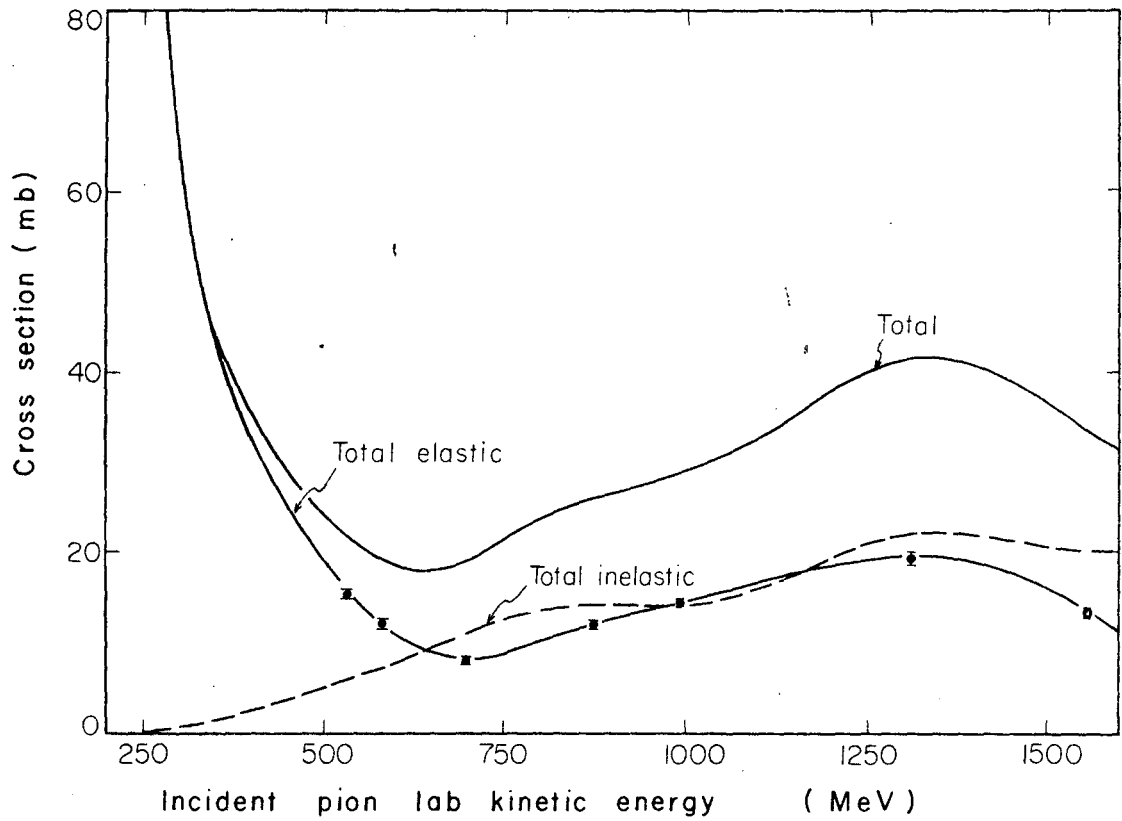
Table XII. Coefficients of powers of $\cos \theta^*$.

Coefficients	Incident pion lab kinetic energy (MeV).						
	533	581	698	873	990	1311	1555
a_0	0.436±0.017	0.336±0.026	0.173±0.014	0.190±0.053	0.184±0.046	0.337±0.052	0.308±0.031
a_1	2.042±0.070	1.745±0.121	0.692±0.049	1.108±0.213	0.528±0.175	-1.266±0.290	0.467±0.175
a_2	2.869±0.101	2.679±0.139	1.960±0.092	3.004±0.621	4.583±0.508	5.272±0.626	1.642±0.397
a_3	0.250±0.250	-0.051±0.377	0.432±0.141	-0.932±1.688	0.920±1.335	-1.235±2.248	-6.322±1.326
a_4	-0.868±0.239	-1.303±0.369	-0.940±0.174	-2.219±1.820	-6.515±1.430	-17.364±1.970	-7.837±1.286
a_5	--	--	--	4.476±3.939	3.607±2.998	10.548±5.072	16.012±2.990
a_6	--	--	--	1.480±1.387	5.237±1.111	20.410±1.764	12.252±1.140
a_7	--	--	--	-3.301±2.611	-3.682±1.978	-2.614±3.415	-4.971±2.068



MUB-1197

Fig. 27. Coefficients of power series in $\cos \theta^*$ plotted vs the incident pion lab kinetic energy.



MUR-1352

Fig. 28. The π^+ -p total cross section, total elastic cross section, and total inelastic cross section plotted vs incident pion lab kinetic energy.

V. DISCUSSION

One of the objectives of this experiment was to determine the quantum numbers of the state that appears to be in "resonance" near 1350 MeV, and the quantum numbers of the state that is the major contributor to the "shoulder" near 850 MeV.

It is difficult to draw any conclusions regarding quantum numbers from a cursory inspection of the differential-cross-section curves (Figs. 19 through 25). However, several aspects of these curves are noteworthy. One point is that the curves at the lower three energies all have similar shapes, and the curves at the higher three energies have a different characteristic shape. The shape of the curve at 873 MeV seems to be a combination of the first shape and the second shape, with probably more characteristics of the higher-energy curves. The fact that the 873-MeV curve seems to be in a transition region may be the reason that such a high (seventh) order fit was needed.

The interesting feature of the higher-energy curves is the sharp rise in the cross sections at $\cos \theta^* = -1$. This sharp rise is most pronounced in the energy region of the 1350-MeV peak, and less pronounced at energies on either side of this peak. The shape of the curve at 1311 MeV (Fig. 24) is somewhat suggestive of a plot of $P_3^2(\cos \theta^*)$, where

$$P_3(\cos \theta^*) = (5/2)\cos^3 \theta^* - (3/2)\cos \theta^* \quad (31)$$

is the third-order Legendre polynomial. A plot of $P_3^2(\cos \theta^*)$ would have a bump at $\cos \theta^* = +0.4$, as well as the one at $\cos \theta^* = -0.4$, and the forward rise at $\cos \theta^* = 1$ would be the same height as the rise at $\cos \theta^* = -1$. As will be shown below, $P_3(\cos \theta^*)$ is related to the partial-wave state with orbital angular momentum $\ell = 3$.

Much additional information can be learned concerning the assignment of quantum numbers by looking at the plots of the coefficients of the powers of $\cos \theta^*$ as shown in Fig. 27. In order to fully understand the information that is available in these plots, it is first necessary to examine the expansion of the π -p differential cross section

in terms of the partial-wave scattering amplitudes,

$$\frac{d\sigma(\theta^*)}{d\Omega^*} = \left| \sum_{\ell=0}^L [(\ell+1)A_{\ell}^+ + \ell A_{\ell}^-] P_{\ell}(\cos \theta^*) \right|^2 + \left| \sum_{\ell=1}^L (A_{\ell}^+ - A_{\ell}^-) P_{\ell}^1(\cos \theta^*) \right|^2. \quad (32)$$

Here A_{ℓ}^{\pm} is the scattering amplitude for the partial wave with orbital angular momentum ℓ and total angular momentum $J = \ell \pm 1/2$. The functions $P_{\ell}(\cos \theta^*)$ and $P_{\ell}^1(\cos \theta^*)$ are the Legendre polynomial and the first associated Legendre polynomial, respectively, of order ℓ . The symbol L represents the maximum value of ℓ that is needed in the sums; i. e., A_{ℓ}^+ and A_{ℓ}^- are both essentially zero if ℓ is greater than L . The partial-wave amplitudes can be written as

$$A_{\ell}^{\pm} = \frac{b_{\ell}^{\pm} \exp(2i\delta_{\ell}^{\pm}) - 1}{2ik}, \quad (33)$$

where k is the wave number in the c.m. system, δ_{ℓ}^{\pm} is the real part of the phase shift, and

$$b_{\ell}^{\pm} = \exp(-2\beta_{\ell}^{\pm}) \quad (34)$$

is the absorption parameter, β_{ℓ}^{\pm} being the imaginary part of the phase shift.

In expanding Eq. (32) it is convenient to use the standard symbols, $S, P, D, F,$ and $G,$ for the scattering amplitudes with $\ell = 0, 1, 2, 3,$ and $4,$ respectively. As an example, if $\ell = 3,$ then $A_3^+ \equiv F_{7/2}$ and $A_3^- \equiv F_{5/2}$. With this notation the expansion of Eq. (32) becomes

$$\begin{aligned}
 \frac{d\sigma(\theta^*)}{d\Omega^*} = & [S_{1/2}^2 - 2S_{1/2}D_{3/2} - 3S_{1/2}D_{5/2} + P_{1/2}^2 - 2P_{1/2}P_{3/2} - 3P_{1/2}F_{5/2} \\
 & + 3P_{1/2}F_{7/2} + P_{3/2}^2 + 3P_{3/2}F_{5/2} - 3P_{3/2}F_{7/2} + D_{3/2}^2 + 3D_{3/2}D_{5/2} \\
 & + (9/4)D_{5/2}^2 + (9/4)F_{5/2}^2 - (9/2)F_{5/2}F_{7/2} + (9/4)F_{7/2}^2] \\
 + \cos \theta^* & [2S_{1/2}P_{1/2} + 4S_{1/2}P_{3/2} - 9S_{1/2}F_{5/2} - 12S_{1/2}F_{7/2} + 4P_{1/2}D_{3/2} \\
 & - 9P_{1/2}D_{5/2} - 10P_{3/2}D_{3/2} + 21D_{3/2}F_{7/2} + (45/2)D_{5/2}F_{5/2} + 9D_{5/2}F_{7/2}] \\
 + \cos^2 \theta^* & [6S_{1/2}D_{3/2} + 9S_{1/2}D_{5/2} + 6P_{1/2}P_{3/2} + 9P_{1/2}F_{5/2} - 30P_{1/2}F_{7/2} \\
 & + 3P_{3/2}^2 - 36P_{3/2}F_{5/2} - 6P_{3/2}F_{7/2} + 3D_{3/2}^2 - 36D_{3/2}D_{5/2} \\
 & - (9/2)D_{5/2}^2 - (9/2)F_{5/2}^2 + (207/2)F_{5/2}F_{7/2} + (45/4)F_{7/2}^2] \\
 + \cos^3 \theta^* & [15S_{1/2}F_{5/2} + 20S_{1/2}F_{7/2} + 15P_{1/2}D_{5/2} + 18P_{3/2}D_{3/2} + 12P_{3/2}D_{5/2} \\
 & + 12D_{3/2}F_{5/2} - 110D_{3/2}F_{7/2} - 117D_{5/2}F_{5/2} - 30D_{5/2}F_{7/2}] \\
 + \cos^4 \theta^* & [35P_{1/2}F_{7/2} + 45P_{3/2}F_{5/2} + 25P_{3/2}F_{7/2} + 45D_{3/2}D_{5/2} \\
 & + (45/4)D_{5/2}^2 + (45/4)F_{5/2}^2 - (675/2)F_{5/2}F_{7/2} - (165/4)F_{7/2}^2] \\
 + \cos^5 \theta^* & [105D_{3/2}F_{7/2} + (225/2)D_{5/2}F_{5/2} + 45D_{5/2}F_{7/2}] \\
 + \cos^6 \theta^* & [150F_{5/2}F_{7/2} + \frac{175}{4}F_{7/2}^2].
 \end{aligned}
 \tag{35}$$

Since the scattering amplitudes are complex quantities, complex multiplication must be used in this equation. For example, $F_{7/2}^2$ means $|F_{7/2}|^2$ and $F_{5/2}F_{7/2}$ means the real part of $F_{5/2}^*F_{7/2}$.

Equation (35) does not include any terms for l greater than three. Although the curve fitting (Sec. IVB) seems to indicate that terms through $\cos^7\theta^*$ are needed at some energies of the experiment, it is believed that the $\cos^7\theta^*$ term results from the superposition of a large F wave and a very small G wave. Therefore, the inclusion of G waves in Eq. (35) would only serve to further complicate the situation. In addition the errors in the coefficients, a_7 , of $\cos^7\theta^*$ (shown in Table XII) are relatively large, being of the same order as the coefficients themselves.

One might wonder why it is not possible to set the terms in Eq. (35) equal to the seven corresponding coefficients in Table XII and solve for the seven scattering amplitudes. The reason is that the scattering amplitudes each have both a real and imaginary part, so there are actually 14 unknown quantities. This is one of the reasons, as mentioned in the Introduction, that additional information, e.g., polarization data, is needed in order to fully analyze pion-proton scattering.

As mentioned before, some information can be gained by examining the coefficients of the powers of $\cos\theta^*$, as plotted in Fig. 27. The most interesting features of this figure are the large positive peak in a_6 and the large negative peak in a_4 , both peaking in the vicinity of the 1350-MeV resonance. By referring to Eq. (35) we see that the large value of a_6 could either come from the $F_{7/2}^2$ term or the $F_{5/2}F_{7/2}$ term. These same terms also appear with the opposite sign in the coefficient of $\cos^4\theta^*$. On the basis of the small magnitudes of the lower four coefficients, a_0 through a_3 , we might assume that the rest of the terms in the coefficient a_4 are negligible, and thereby determine the relative magnitudes of $F_{7/2}^2$ and $F_{5/2}F_{7/2}$ at 1350 MeV. Taking $a_6 = 21$ mb/sr and $a_4 = -18$ mb/sr from Fig. 27, we can calculate that $F_{7/2}^2$ is approximately twice as large as $F_{5/2}F_{7/2}$. This seems to be good evidence for saying that the 1350-MeV resonance is an $F_{7/2}$ resonance.

Unfortunately, the Minami ambiguity¹⁶ must be considered. i.e. with differential-cross-section data alone, one cannot tell whether the resonance is really an $F_{7/2}$ resonance or whether it might be a $G_{7/2}$ resonance. In essence, the Minami ambiguity says that if the values of the two scattering amplitudes for the two ℓ values with a particular J value are interchanged for all values of J , then the differential cross section will be unchanged. This means that the simultaneous interchange of $S_{1/2}$ with $P_{1/2}$, $P_{3/2}$ with $D_{3/2}$, $D_{5/2}$ with $F_{5/2}$, $F_{7/2}$ with $G_{7/2}$, etc. will leave $d\sigma/d\Omega^*$ unaffected.

There are at least two reasons for favoring the $F_{7/2}$ assignment over $G_{7/2}$. First, if the 1350-MeV resonance is a true elastic resonance analogous to the $(3, 3)$ resonance, i.e., there is an intermediate state consisting of a single particle, it is reasonable to assume that this intermediate particle is an excited nucleon, and hence should have the same parity as the nucleon. It is the $F_{7/2}$ pion-proton state which has positive parity. Another reason for favoring the $F_{7/2}$ assignment is that it agrees with the Regge-pole formalism as presented by Chew and Frautschi.¹⁷ They seem to believe that the 1350-MeV resonance has the same parity as the $(3, 3)$ resonance, which again is positive.

In summary, it can be concluded that the resonance near 1350 MeV has $J = 7/2$, $\ell = 3$, isotopic spin $T = 3/2$, and positive parity. The mass of the resonant-state particle is approximately 1920 MeV.

There does not appear to be any single state which is very prominent at the shoulder near 850 MeV. Looking at Fig. 27 we see a very small bump in a_5 near 850 MeV, but the errors on the data points are so large that it is questionable whether or not this bump really exists. The total elastic and inelastic cross sections are plotted in Fig. 28. The behavior of the total inelastic cross section near 850 MeV is similar to that needed in the Ball-Frazer⁴ explanation of peaks in total cross sections. In view of these facts, it can be suggested that the shoulder near 850 MeV is the result of an inelastic enhancement rather than an elastic resonance. It is quite probable that this inelastic process, which produces the shoulder near 850 MeV in the $T = 3/2$ ($\pi^+ - p$) total cross section, is the same inelastic process that contributes to the $\pi^- - p$ peak at 900 MeV,^{1, 3} since $\pi^- - p$ scattering is a mixture of $T = 3/2$ and $T = 1/2$ interactions.

ACKNOWLEDGMENTS

Special thanks are due to Professor Burton J. Moyer, not only for his guidance in the performance of this experiment, but also for the invaluable assistance and counsel that he has provided the author throughout several years of graduate study.

The author is greatly indebted to many people for the success of this experiment:

To Dr. Michael J. Longo, Dr. Calvin D. Wood, Dr. Thomas J. Devlin, Jr., and Mr. Donald E. Hagge, who did much for the experiment by contributing both useful suggestions and many hours of hard work.

To Mr. Robert Profet, Mr. Dale Dickinson, and Mr. Burns Macdonald for their considerable assistance in the performance of this experiment.

To Dr. Robert W. Kenney for many extremely helpful and stimulating discussions.

To Mr. Dick Mack and the people working with him, for assistance with the electronics in the experiment—especially Mr. Larry Scott, who designed much of the special circuitry used in the experiment, Mr. Fung Gin, who helped build and maintain this circuitry, and Mr. Fred Kirsten and Mr. Leonard Proehl for designing and building a special test system used in the experiment.

To the people in the engineering department, particularly Mr. Jim Fiedler, who was responsible for the overall setup of the experiment, and Mr. George Edwards and Mr. Bob Edwards, for their help with the velocity spectrometer and Bevatron target, respectively.

To Mr. Roy Loop and Mr. Jim Minter for taking care of the magnets and their power supplies.

To the many people who worked on the hydrogen target.

To the Bevatron staff and crew under the direction of Dr. Edward J. Lofgren, especially Mr. Wendell Olson and Mr. Bob Pratt, who did an excellent job of setting up the experiment.

To Mr. Leo Leidy for building special equipment used in the experiment.

To Mr. Jay Spoonheim for assembling some of the equipment.

To the people in the computer group and the data analysts for their assistance in processing the data.

In addition the author would like to thank those people who helped put this thesis in final form, especially Mr. Stan Lerner, for his help with preliminary editing and typing, and Professor A. C. Helmholtz, for many helpful suggestions.

The author owes his greatest debt of gratitude to his wife, Dorothy for her patient endurance and encouragement during the sometimes difficult and occasionally frustrating years leading to the completion of this work.

This work was done under the auspices of the U. S. Atomic Energy Commission.

APPENDICES

A. Momentum Determination

Several different methods were employed in determining the momenta of the experiment and a least-squares average of the results was calculated; i. e. , a curve having an equation $y = \text{constant}$ was least-squares-fitted to the data. (An arbitrary number assigned to each method was used as the abscissa.) The various methods and their numbers are:

- (1) First wire-orbit momentum determination
- (2) Second wire-orbit momentum determination
- (3) Third wire-orbit momentum determination
- (4) Time-of-flight measurement
- (5) OPTIK⁸
- (6) Velocity-spectrometer magnetic-field values
- (7) Gas Cerenkov counter pressure curves.

The ratios of the momenta determined by each method to the average momenta are listed below, along with the associated errors.

Number of method	Determined momenta average momenta
1	1.004±0.0085
2	1.001±0.0061
3	0.999±0.0061
4	0.993±0.0052
5	1.036±0.0233
6	1.046±0.1412
7	1.057±0.0429
Average	1.000±0.0110

The first wire orbit differed from the second and third because a large block of iron had not yet been put in place between B_2 and Q_4 for the first wire orbit (see Fig. 2). Although this block of iron had a large hole for the beam to pass through, the effective field strength of B_2 was reduced by about 2.2%. This additional correction factor increased the error in the first wire-orbit determination as compared to the error in the second or third wire orbit. The main errors in the wire orbits are based on repeatability of measurements within each of the three wire-orbit momentum determinations.

The time-of-flight method was based on measuring the difference in time of flight between pions and protons in the beam. With a momentum of about 700 MeV/c the difference in time of flight from counter M_1 to counter M_3 was about 30 nsec. By accurately measuring the time difference, the momentum of the beam can be calculated. The difficulty in this method is in determining the velocity of the signal in the cable that was used. The errors in this method reflect the uncertainty in this velocity.

The fifth method used the IBM 7090 program OPTIK.⁸ In this method the settings of the magnets at which the pion beam flux was maximized were fed into OPTIK along with various momenta. By examining the corresponding positions of the final focal points in both planes, the momentum corresponding to the best overall focus was determined. The errors are related to the fact that with the given input OPTIK was unable to produce a focus in both planes simultaneously, hence there was a range of momentum that was acceptable.

In the sixth method, the velocity-spectrometer method, it was necessary to know the ratio of the magnetic field strength needed for undeflected pions to the magnetic field strength needed for undeflected protons in the velocity spectrometer, assuming constant electric field strength. This ratio is equal to the ratio of the velocity of the proton to the velocity of the pion. By knowing the ratio of velocities it is possible to calculate the momentum. This method is the least accurate.

method, due to large uncertainties in the magnitudes of the magnetic field strengths.

In the last method the pressure thresholds for counting muons and pions were determined from the Cerenkov curves (see Fig. 15). By knowing the index of refraction of the gas at these pressures it was possible to determine the momentum of the muons and pions in the beam. Large uncertainties came from both the location of the pressure thresholds and the index-of-refraction determinations.

B. Velocity-Spectrometer Equation

When the velocity spectrometer is properly adjusted, such that the pions are undeflected as they pass through it, the beam of protons is bent an angle α . The straight-line backward extension of the proton beam, after being bent, intersects the pion beam at the center of the spectrometer. The equation for the angle of bend of the proton beam is

$$\alpha = \left(\frac{V}{\gamma_p m_p} \right) \left(\frac{L}{d} \right) \left(\frac{\beta_\pi - \beta_p}{\beta_\pi \beta_p} \right), \quad (B-1)$$

where

α is in radians,

V is the voltage across the electric plates in kV,

m_p is the rest mass of the proton in keV,

γm_p is the relativistic mass of the proton in keV,

L is the effective length of the fields in the spectrometer in inches,

d is the gap width in inches,

β_π is (the velocity of the pion/velocity of light in a vacuum).

and

β_p is (the velocity of the proton/velocity of light in a vacuum).

REFERENCES

1. (a). C. D. Wood, T. J. Devlin, J. A. Helland, M. J. Longo, B. J. Moyer, and V. Perez-Mendez, Phys. Rev. Letters 6, 481 (1961).
(b). J. A. Helland, T. J. Devlin, D. E. Hagge, M. J. Longo, B. J. Moyer, V. Perez-Mendez, and C. D. Wood, Elastic Scattering of Negative Pions on Protons in the Energy Range 500 to 1000 MeV, Lawrence Radiation Laboratory Report UCRL-10495 (to be submitted to Phys. Rev.).
See also references cited in 1(a) above.
2. (a). U. Bidan, F. Levy, N. Abbattista, A. Minafra, S. Morganti, A. Romano, and P. Wołoszek, Nuovo Cimento 24, 334 (1962).
(b). R. Barloutaud, C. Choquet-Louedec, A. Derem, J. Heughebaert, A. Leveque and J. Meyer, Phys. Rev. Letters 1, 207 (1962).
(c). J. K. Kopp, A. M. Shapiro, and A. R. Erwin, Phys. Rev. 123, 301 (1961).
(d). L. O. Roellig and D. A. Glaser, Phys. Rev. 116, 1001 (1959).
(e). B. J. Malenka and H. S. Valk, Phys. Rev. 122, 934 (1961).
(f). W. J. Willis, Phys. Rev. 116, 753 (1959).
3. See for example:
(a). H. C. Burrowes, D. O. Caldwell, D. H. Frisch, D. A. Hill, D. M. Ritson, R. A. Schluter, and M. A. Wahlig, Phys. Rev. Letters 2, 119 (1959).
(b). T. J. Devlin, B. J. Moyer, and V. Perez-Mendez, Phys. Rev. 125, 690 (1962).
(c). J. C. Brisson, J. F. Detoeuf, P. Falk-Varrant, L. Van Rossum, and G. Valladas, Nuovo Cimento 19, 210 (1961).
(d). M. J. Longo, J. A. Helland, W. N. Hess, B. J. Moyer, and V. Perez-Mendez, Phys. Rev. Letters 3, 568 (1959).
4. J. S. Ball and W. R. Frazer, Phys. Rev. Letters 3, 201 (1959).
5. E. F. Beall, B. Cork, P. G. Murphy, W. A. Wenzel, G. M. Peck, Johnson, and L. J. Koester, Jr., Phys. Rev. 126, 1551 (1962) and references cited therein.

6. J. C. Brisson, P. Falk-Vairant, J. P. Merlo, P. Sonderegger, R. Turlay, and G. Valladas, CEN Saclay Report 61-8 (1961) (unpublished) and references cited therein.
7. F. P. Dixon and R. L. Walker, Phys. Rev. Letters 1, 458 (1958) and references cited therein.
8. T. J. Devlin, Lawrence Radiation Laboratory Report UCRL-9727, Sept. 1961 (unpublished).
9. D. B. Chelton and D. B. Mann, University of California Radiation Laboratory Report UCRL-3421, May 1956 (unpublished).
10. Lawrence Radiation Laboratory Counting Handbook, UCRL-3307 Rev., Jan. 1959 (unpublished).
11. L. Scott, Lawrence Radiation Laboratory Report UCID-1597, Oct. 1961 (unpublished).
12. W. A. Wenzel, University of California Radiation Laboratory Report UCRL-8000, Oct. 1957 (unpublished).
13. J. Atkinson and V. Perez-Mendez, Rev. Sci. Instr. 30, 865 (1959).
14. P. Cziffra and M. J. Moravcsik, Lawrence Radiation Laboratory Report UCRL-8523 Rev., June 1959 (unpublished).
15. See for example: J. W. Cronin, Phys. Rev. 118, 824 (1960).
16. S. Minami, Prog. Theoret. Phys. (Kyoto) 11, 213 (1954).
17. G. F. Chew and S. C. Frautschi, Phys. Rev. Letters 8, 41 (1962).

